

Phosphorylation-Driven Epichaperome Assembly: A Critical Regulator of Cellular Adaptability and Proliferation

Gabriela Chiosis

`chiosisg@MSKCC.ORG`

Memorial Sloan Kettering Cancer Center <https://orcid.org/0000-0003-0486-6920>

Seth McNutt

University of New Hampshire

Tanaya Roychowdhury

MSKCC

Chiranjeevi Pasala

Memorial Sloan Kettering Cancer Center

Hieu Nguyen

University of New Hampshire

Daniel Thorton

University of New Hampshire

Sahil Sharma

Memorial Sloan Kettering Cancer Center <https://orcid.org/0000-0001-7281-9224>

Luke Boticelli

University of New Hampshire

Chander Digwal

MSKCC <https://orcid.org/0000-0001-8784-1096>

Sahasini Joshi

Memorial Sloan Kettering Cancer Center

Nan Yang

University of New Hampshire

palak panchal

mskcc

Souparna Chakrabarty

Memorial Sloan Kettering Cancer Center

Sadik Bay

Memorial Sloan Kettering Cancer Center <https://orcid.org/0000-0001-8089-1330>

Vladimir Markov

Memorial Sloan Kettering Cancer Center

Charlene Kwong

Memorial Sloan Kettering Cancer Center

Jeanine Lisanti

Memorial Sloan Kettering Cancer Center

Sun Young Chung

Harvard Medical School <https://orcid.org/0000-0002-3381-919X>

Stephen Ginsberg

NYU <https://orcid.org/0000-0002-1797-4288>

Pengrong Yan

Memorial Sloan Kettering Cancer Center

Elisa de Stanchina

Memorial Sloan Kettering Cancer Center

Adriana Corben

MSKCC

Shanu Modi

Memorial Sloan Kettering Cancer Center

Mary Alpaugh

Memorial Sloan Kettering Cancer Center <https://orcid.org/0000-0002-0008-2718>

Giorgio Colombo

University of Pavia <https://orcid.org/0000-0002-1318-668X>

Hediye Erdjument-Bromage

New York University Grossman School of Medicine

Thomas Neubert

NYU Langone

Robert Chalkley

University of California, San Francisco <https://orcid.org/0000-0002-9757-7302>

Peter Baker

UCSF

Alma Burlingame

University of California <https://orcid.org/0000-0002-8403-7307>

Anna Rodina

Sloan Kettering Institute <https://orcid.org/0000-0002-3894-6438>

Feixia Chu

University of New Hampshire <https://orcid.org/0000-0002-3209-8095>

Article

Keywords:

Posted Date: April 3rd, 2024

DOI: <https://doi.org/10.21203/rs.3.rs-4114038/v1>

License:  This work is licensed under a Creative Commons Attribution 4.0 International License.

[Read Full License](#)

Additional Declarations: **Yes** there is potential Competing Interest. Memorial Sloan Kettering Cancer Center holds the intellectual rights to the epichaperome portfolio. G.C., A.R. and S.S. are inventors on the licensed intellectual property. All other authors declare no competing interests.

1 Phosphorylation-Driven Epichaperome Assembly: A Critical Regulator of Cellular Adaptability
2 and Proliferation

3 Seth W. McNutt^{1,12}, Tanaya Roychowdhury^{2,12}, Chiranjeevi Pasala², Hieu T. Nguyen¹, Daniel T.
4 Thornton¹, Sahil Sharma², Luke Botticelli¹, Chander S. Digwal², Suhasini Joshi², Nan Yang¹, Palak
5 Panchal², Souparna Chakrabarty², Sadik Bay², Vladimir Markov³, Charlene Kwong³, Jeanine Lisanti³, Sun
6 Young Chung², Stephen D. Ginsberg^{4,5}, Pengrong Yan², Elisa DeStanchina³, Adriana Corben⁶, Shanu
7 Modi⁷, Mary Alpaugh², Giorgio Colombo⁸, Hediye Erdjument-Bromage⁹, Thomas A. Neubert⁹, Robert J.
8 Chalkley¹⁰, Peter R. Baker¹⁰, Alma L. Burlingame¹⁰, Anna Rodina², Gabriela Chiosis^{2,7,13}, Feixia Chu^{1,11,13}

9

10 1. Department of Molecular, Cellular & Biomedical Sciences, University of New Hampshire, Durham, NH
11 03824, USA.

12 2. Chemical Biology Program, Memorial Sloan Kettering Cancer Center, New York, NY 10065, USA.

13 3. Antitumor Assessment Core Facility, Memorial Sloan Kettering Cancer Center, New York, NY 10065,
14 USA.

15 4. Departments of Psychiatry, Neuroscience & Physiology & the NYU Neuroscience Institute, NYU
16 Grossman School of Medicine, New York, NY, 10016, USA.

17 5. Center for Dementia Research, Nathan Kline Institute, Orangeburg, NY, 10962, USA.

18 6. Department of Pathology, Memorial Sloan Kettering Cancer Center, New York, NY, 10065, USA.

19 7. Department of Medicine, Division of Solid Tumors, Memorial Sloan Kettering Cancer Center, New York,
20 NY 10065, USA.

21 8. Department of Chemistry, University of Pavia, via Taramelli 12, 27100 Pavia, Italy.

22 9. Department of Neuroscience and Physiology and Neuroscience Institute, NYU Grossman School of
23 Medicine, New York, NY, 10016, USA.

24 10. Mass Spectrometry Facility, University of California, San Francisco, California 94143, USA.

25 11. Hubbard Center for Genome Studies, University of New Hampshire, Durham, NH 03824, USA.

26 ¹²co-first author, equally contributed to the work.

27 ¹³These authors jointly supervised this work: Feixia Chu, Gabriela Chiosis.

28 *Correspondence: feixia.chu@unh.edu (F.C.), chiosisg@mskcc.org (G.C.).

29

30

31 **Abstract.** The intricate protein-chaperone network is vital for cellular function. Recent discoveries
32 have unveiled the existence of specialized chaperone complexes called epichaperomes, protein
33 assemblies orchestrating the reconfiguration of protein-protein interaction networks, enhancing
34 cellular adaptability and proliferation. This study delves into the structural and regulatory aspects
35 of epichaperomes, with a particular emphasis on the significance of post-translational
36 modifications in shaping their formation and function. A central finding of this investigation is the
37 identification of specific PTMs on HSP90, particularly at residues Ser226 and Ser255 situated
38 within an intrinsically disordered region, as critical determinants in epichaperome assembly. Our
39 data demonstrate that the phosphorylation of these serine residues enhances HSP90's interaction
40 with other chaperones and co-chaperones, creating a microenvironment conducive to
41 epichaperome formation. Furthermore, this study establishes a direct link between epichaperome
42 function and cellular physiology, especially in contexts where robust proliferation and adaptive
43 behavior are essential, such as cancer and stem cell maintenance. These findings not only
44 provide mechanistic insights but also hold promise for the development of novel therapeutic
45 strategies targeting chaperone complexes in diseases characterized by epichaperome
46 dysregulation, bridging the gap between fundamental research and precision medicine.

47

1 Introduction

2 Conventional wisdom, as crystallized in Beadle and Tatum's 1941 paradigm of "one gene—one
3 enzyme—one function," has traditionally delineated targets as outcomes of protein expression
4 changes or point mutations within proteins. However, it is increasingly apparent that protein
5 dysfunctions in the context of many disorders, including cancer, neurodegenerative disorders,
6 among others, are predominantly shaped by changes in interaction strengths and cellular
7 mislocalization. These factors, in turn, can be modulated by variations in post-translational
8 modifications (PTMs), stabilization of disease-associated protein conformations, and other
9 protein-modifying mechanisms^{1,2}. Within this complex context, Heat Shock Protein 90 (HSP90)
10 emerges as a compelling exemplar, transcending the boundaries of conventional understanding³.

11 Positioned as a versatile chaperone, often referred to as the guardian of the proteome, HSP90
12 assumes a pivotal task in the realm of maintaining cellular equilibrium by facilitating protein
13 folding, stabilization, and degradation⁴. Under the canonical folding paradigm, HSP90 functions
14 as a homodimer. Each protomer is composed of an N-terminal domain (NTD), a middle domain
15 (MD), and a C-terminal dimerization domain (CTD)^{4,5}. The NTD contains a nucleotide binding
16 pocket, where ATP binding and hydrolysis takes place⁶. The chaperone cycle of HSP90 is coupled
17 to a series of dynamic conformational changes accompanying its ATPase cycle. Beginning with
18 NTD/MD and MD/CTD interdomain rotations and cross-monomer dimerization⁷, HSP90
19 transitions from open to closed conformational states, while folding client proteins^{8,9}. HSP70 and
20 HOP (HSP70-HSP90 organizing protein) bring client proteins to HSP90 and form the loading
21 complex¹⁰. Other co-chaperones participate at different stages of the HSP90 chaperone cycle and
22 regulate its conformational changes along the chaperone and ATPase cycle⁴. Co-chaperones
23 may have different preferences for client proteins, fine-tuning subcellular pools of HSP90 to
24 mitigate stressors and maintain proteostasis¹¹. These assemblies are further shaped by PTMs in
25 HSP90, co-chaperones and client proteins¹². Overall, the highly orchestrated interactions among
26 these proteins – both chaperones and clients – are transient in the chaperone cycle under
27 physiological conditions.

28 While this classical understanding portrays HSP90 as a dimeric entity that interacts dynamically
29 with co-chaperones and client proteins, research has uncovered a spectrum of multimeric HSP90
30 forms, each sculpted by the cellular milieu and the presence of stress-inducing factors³. These
31 multimers, whether homo-oligomeric or hetero-oligomeric, expand HSP90's functional repertoire,
32 blurring the boundaries between traditional chaperone functions and newfound roles as holdases
33 or scaffold proteins. In disease contexts, such as cancer and neurodegenerative disorders,
34 HSP90's conformational adaptability gives rise to epichaperomes—distinctive hetero-oligomeric
35 formations of tightly bound chaperone, co-chaperones and other factors¹³⁻¹⁵. This phenomenon
36 goes beyond mere biochemical curiosity; it represents a fundamental mechanism by which cells
37 respond to stressors, whether of genetic, proteotoxic or environmental nature^{3,16-18}. Unlike
38 chaperones which help proteins fold or assemble, epichaperomes exert a maladaptive influence,
39 reshaping the assembly and connectivity of proteins pivotal for sustaining pathological traits. For
40 example, in cancer, epichaperomes take on scaffolding functions not found in normal cells,
41 altering the assembly and connectivity of proteins important for maintaining a malignant
42 phenotype and enhancing their activity, which provides a survival advantage to cancer cells and
43 tumor-supporting cells^{13,19}. In Alzheimer's disease epichaperomes rewire the connectivity of, and
44 thus negatively impact, proteins integral for synaptic plasticity, brain energetics and immune
45 response¹⁵.

46 The revelation of HSP90's maladaptive multimeric epichaperomes has also profound implications
47 for therapeutic interventions, including in the treatment of diverse disease states including cancers
48 and of neurodegenerative disorders. Rather than a blanket inhibition of all HSP90 pools, targeting

1 specific pathologic conformations of HSP90 as found in epichaperomes while sparing normal
2 HSP90 functions holds the promise of enhancing the safety as well as the immunostimulatory and
3 anticancer effects of HSP90 inhibitors³.

4 Despite these important mechanistic and therapeutic implications, key factors facilitating HSP90
5 incorporation in epichaperomes – namely the conformations that enable epichaperome formation
6 and structural elements that support the enrichment of such conformation - remain unknown. In
7 this study, we use a combination of chemical biology and unbiased mass spectrometry techniques
8 to elucidate the conformation of HSP90 populated in epichaperomes and to characterize
9 molecular factors that support and favor the enrichment of such conformation. Beyond structural
10 revelations, our findings demonstrate how these factors directly influences cellular behaviors,
11 particularly in contexts where robust proliferation and adaptation are crucial, such as cancer and
12 stem cell maintenance. This direct link between epichaperome function and fundamental cellular
13 processes has translational relevance for therapeutic development.

14 **RESULTS**

15 **Pluripotent stem cells and cancer cells share epichaperomes**

16 Epichaperomes nucleated through enhanced interactions between HSP90 and HSP70, namely
17 the heat shock cognate 70 (HSC70) isoform, are a distinct feature of cancer cells^{13,19}.
18 Epichaperomes containing HSP90 are detected in iPSCs (induced pluripotent stem cells)²⁰, in
19 leukemia stem cells^{21,22} and in glioma cancer stem cells (CSCs)²³. Hyperactivation of the
20 transcription factor c-MYC required in generating iPSCs²⁴, maintaining embryonic stem cells
21 (ESCs)²⁵ and CSCs²⁶, is also a driving factor in epichaperome formation in tumors, irrespective
22 of the tumor type^{13,27}. Notably, these epichaperomes are all sensitive to and can be disrupted by
23 small molecules such as PU-H71 (zelavespib) or PU-AD (icapamespib) that bind to HSP90^{13,23,28},
24 suggesting that a similar composition, facilitated by a specific conformation of HSP90, may
25 characterize epichaperomes in these distinct cellular contexts.

26 To test this hypothesis, we initially explored the composition of epichaperomes in selected cellular
27 models, encompassing pluripotent stem cells and cancer cells. For pluripotent stem cells, we
28 examined two mouse embryonic stem cell lines (E14 and ZHBTc4) and a human induced
29 pluripotent cell line (hiPSC). Additionally, two cancer cell lines, well-characterized in terms of
30 epichaperome composition and function, were chosen as representative epichaperome-positive
31 (MDA-MB-468) and -negative/low (ASPC1) cancer cells (**Fig. 1a-f and Supplementary Figs.**
32 **1,2**).

33 In contrast to folding chaperone complexes, which are inherently dynamic and short-lived⁶,
34 epichaperomes represent long-lasting heterooligomeric assemblies composed of tightly
35 associated chaperones, co-chaperones, and various other factors. HSP90 is a major component
36 found within epichaperomes along with other chaperones, co-chaperones, and scaffolding
37 proteins like HSP70 (especially HSC70), CDC37, AHA1, and HOP¹³. Consequently, when we
38 analyzed cell homogenates containing epichaperomes using native PAGE followed by
39 immunoblotting with antibodies specific to epichaperome constituent chaperones and co-
40 chaperones, we observed a range of high-molecular-weight species, both distinct and indistinct,
41 in addition to the primary band(s) characteristic of chaperones. This observation held true for both
42 pluripotent stem cells and cancer cells (**Fig. 1b, Supplementary Fig. 1a-d** and refs. ^{13,19,20}).
43 Notably, HSP90 immunoblotting revealed the presence of species comprising HSP90 in
44 epichaperome assemblies in cancer cells and pluripotent stem cells, in addition to the prominent
45 242 kDa band, which is a characteristic of non-transformed cells^{13,19,29}.

1 Epichaperomes undergo disassembly during iPSC differentiation²⁰ or when cancer cells are
2 treated with PU-H71 or PU-AD^{15,23,28,30}. Therefore, next we induced the differentiation of the
3 pluripotent stem cells under investigation. In the ZHBTc4 cell line, Oct4 expression is controlled
4 by a Tet (tetracycline)-*off oct4* regulatory system³¹. Down-regulation of Oct4 in ZHBTc4 cells has
5 been reported to induce trophoblast differentiation, which is characterized by changes in cell
6 morphology, specifically, cells flattening into epithelial-like cells, and is associated with slower
7 growth³². Mouse embryonic E14 stem cells undergo spontaneous differentiation into embryoid
8 bodies when cultured in suspension without antidifferentiation factors such as leukemia inhibitory
9 factor³³ and induced pluripotent stem cells differentiate into mature dopaminergic neurons using
10 a floor-plate based differentiation protocol³⁴. We confirmed that differentiation of these pluripotent
11 stem cells was correlated with the disassembly of epichaperomes, as observed through native
12 PAGE immunoblotting. This disassembly is evident by a reduction in high-molecular-weight
13 chaperone species on native PAGE observed when immunoblotting for epichaperome constituent
14 chaperones (see HSP90 α/β , HOP, HSC70, CDC37, AHA1, HSP110 in **Fig. 1b and**
15 **Supplementary Fig. 1**), with minimal changes observed in total chaperone levels on SDS PAGE.
16 Notably, for HSP90, a decrease in bands other than those in the ~242 kDa range was observed
17 upon differentiation, supportive of epichaperome disassembly (see HSP90 immunoblotting).

18 PU-H71 serves as an epichaperome probe that, in contrast to the tested antibodies which
19 indiscriminately detect epichaperomes and other HSP90 pools, exhibits a preference for HSP90
20 when it is integrated into epichaperomes¹³. Labeled derivatives of PU-H71 can, therefore, be
21 employed to detect HSP90 within epichaperomes, distinguishing it from other HSP90 pools (as
22 illustrated in **Fig. 1c and Supplementary Fig. 2a-c**). To achieve this, we generated lysates from
23 ZHBTc4, E14 cells, and MDA-MB-468 cells under conditions that preserve native protein
24 assemblies. Subsequently, we labeled these homogenates with a clickable PU-probe (PU-TCO,
25 ref. 19). After running these labeled samples on native PAGE gels, we conjugated the PU-probe
26 with a Cy5 dye and visualized epichaperomes, confirming the presence of epichaperomes in both
27 the ESCs and the cancer cells. These epichaperomes were characterized by multimers observed
28 at and above ~300 kDa (**Fig. 1c**). Moreover, the labeling of epichaperomes by the PU-probe
29 decreased upon ESC differentiation, supportive of epichaperome disassembly (**Fig. 1c and**
30 **Supplementary Fig. 2b**).

31 Additionally, we conducted labeling experiments using live E14 ESCs, instead of homogenates,
32 employing a PU-CW800 probe (a derivative of PU-H71 conjugated with an 800 nm near-infrared
33 dye) or a control derivative (an inactive PU-derivative that does not interact with epichaperomes)
34 (see **Supplementary Note 1**). The most responsive target of the PU-probes, but not the control
35 probe, was an HSP90 assembly of approximately 300 kDa, thus above the major 242 kDa band
36 preferred by the anti-HSP90 antibody. This species was detected on Native-PAGE in PU-probe
37 treated cell lysates but not in control treated cell lysates (**Supplementary Fig. 2c**).

38 In summary, the predominant HSP90 band characteristic of epichaperomes is a 300 kDa
39 assembly, distinctly differing from the typical ~242 kDa band observed in non-transformed cells¹³,
40 ^{19, 32} when analyzed on native PAGE gels. Mass spectrometric (MS) analysis of the ~300 kDa
41 assembly confirmed the presence of HSP90 and HSC70 as the primary protein components of
42 this multimeric complex (**Supplementary Data 1**, 300 kDa LC-MS). This finding aligns with the
43 composition of core epichaperome complexes previously reported in cancer cells¹³.
44 Consequently, these findings combined confirm that both cancer cells and pluripotent stem cells
45 share HSP90 and HSC70 as integral constituents of their core epichaperomes.

46 To gain further insights into epichaperome assemblies, we employed resin-based affinity
47 purification experiments. Specifically, we utilized resins with immobilized PU-H71, referred to as
48 PU-beads, and an inert control molecule on control beads, following established procedures¹³

1 (Fig. 1d). As an additional control, we employed a resin containing immobilized geldanamycin
2 (GA), known for its ability to bind and isolate predominantly un-complexed HSP90 (GA-beads,
3 **Supplementary Fig. 3** and ref.³⁵). Subsequently, we subjected the protein cargo isolated by these
4 probes to unbiased MS analysis. To precisely determine the protein components of the cargo, we
5 conducted in-gel digestion of the entire gel lanes and employed liquid chromatography/mass
6 spectrometry (LC-MS/MS) in conjunction with the semi-quantitative spectra-counting method^{36,37}
7 for the identification and quantification of cargo proteins (**Supplementary Data 1**).

8 We observed that the cargo isolated by PU-beads from ESCs contained 26 of the 42 major
9 chaperone and co-chaperones identified prior in cancer cells¹³ as being epichaperome
10 components (**Fig. 1d**). The interaction between PU-beads and epichaperomes was specific
11 towards PU-H71, because control resins did not purify noticeable protein complexes. Similarly,
12 GA-beads precipitated HSP90 but few co-purifying proteins and epichaperome components
13 (**Supplementary Fig. 3, Supplementary Data 1**) consistent with previous results that GA isolates
14 largely an un-complexed HSP90³⁸.

15 In mammalian cells, HSP90 exists in two paralogs, HSP90 α and HSP90 β ³⁹, both of which have
16 been reported to play roles in epichaperome formation in cancer cells¹³. To assess the isoform
17 composition of HSP90 within epichaperomes, we exploited the subtle difference between one pair
18 of isobaric peptides, namely 88Thr-Lys100 in HSP90 α and 83Thr-Lys95 in HSP90 β , where a
19 single amino acid distinguishes them (Ile in HSP90 α and Leu in HSP90 β) (**Supplementary Fig.**
20 **4a**). The assignment of HSP90 isoforms relied on co-eluting peptides obtained from the isobaric
21 peptide present in purified HSP90 β (**Supplementary Fig. 4b,c**). Extracted ion chromatograms of
22 the peptide mass revealed an approximate $\sim 1.5 \beta/\alpha$ ratio in the ESC lysate and the cargo isolated
23 by PU-beads (**Fig. 1e**), while the GA-beads cargo exhibited a $\sim 1.0 \beta/\alpha$ ratio. Similar findings were
24 obtained through spectra counting, with the HSP90 β /HSP90 α ratio determined using spectral
25 counting consistent with ratios obtained through MS intensity calculations (**Supplementary Data**
26 **1: 708/540 = 1.31** for the PU-beads cargo; **219/235 = 0.93** for the GA-beads cargo). This validation
27 of spectra counting as an effective semi-quantitative method supports the conclusion that
28 epichaperomes isolated from ESCs exhibit a predominantly unbiased HSP90 paralog
29 composition, akin to what has been reported for cancer cells¹³.

30 In summary, the wealth of complementary biochemical experiments presented here lends strong
31 support to the idea that both cancer cells and pluripotent stem cells harbor epichaperomes that
32 are compositionally similar. Notably, HSP90 and HSC70 emerge as major constituents of the core
33 epichaperome structure, serving as a scaffold for recruiting various co-chaperones to create
34 specific epichaperome assemblies. This shared architectural similarity between epichaperomes
35 in ESCs and cancer cells underscores the existence of a common epichaperome-enabling HSP90
36 conformer that is enriched in both biological contexts.

37 **Epichaperome-enabling conformation of HSP90**

38 MS identification of cross-linked residues that are in spatial proximity but not necessarily close in
39 primary sequence, provides valuable distance restraints that can be employed for computational
40 modeling of proteins and protein complexes⁴⁰⁻⁴². Therefore, to determine the conformation of
41 HSP90 in epichaperomes, we used a chemical cross-linking and mass spectrometry (CX-MS)
42 approach to identify and quantify cross-linked peptides of PU-H71-favored HSP90 pools.

43 To ensure the capture of the epichaperome-enabling conformation, we first cross-linked cellular
44 lysates using the amine-reactive cross-linker DSS (disuccinimidyl suberate) prior to HSP90
45 capture on the PU-beads^{13,35} (**Fig. 2a**). Parallel experiments were conducted using GA-beads,
46 corresponding to solid-support immobilized GA, as a control^{13,35}. The identity of cross-linked

1 HSP90 peptides purified by PU- or GA-beads pull-down can be found in **Supplementary Data 2**.
2 Notably, the alpha carbon distances between all cross-linked residues, as identified with high
3 confidence, fell below the maximal span of DSS (30 Å). This suggests that proteins retained their
4 native states without significant conformational perturbations during the cross-linking process.

5 We calculated the cross-linking percentage for each pair of cross-linked PU- or GA-bound HSP90
6 residues. This calculation involved normalizing the MS ion intensity of cross-linked peptides by
7 the sum of all cross-linked peptides and cross-linker-modified peptides containing the cross-linked
8 residues. By doing so, we could mitigate the impact of variations in the reactivity of cross-linked
9 residues, allowing us to primarily assess the influence of the distance between cross-linked
10 residues and their local secondary structures⁴³.

11 Most cross-linked pairs from both PU- and GA-bound samples exhibited similar cross-linking
12 percentages, with data points evenly distributed around a trend line with a slope of 1 (dotted line,
13 **Fig. 2b**). This observation suggests a broad similarity in secondary and tertiary structures
14 between these HSP90 populations. However, clear differences emerged, revealing
15 conformational distinctions between the PU- and GA-favored HSP90 subpopulations (highlighted
16 by orange circles, **Fig. 2b**).

17 Notably, residues Lys58-Lys112 in HSP90 α and Lys53-Lys107 in HSP90 β , situated within the
18 ligand-binding pocket, displayed a higher cross-linking percentage in PU-bound HSP90
19 populations compared to their GA-bound counterparts (**Fig. 2b**). This observation aligns with
20 distinct pocket configurations preferred by each ligand, as previously observed through X-ray
21 crystallography⁴⁴⁻⁴⁸. Specifically, crystal structures show the bulkier GA binds more superficially,
22 causing helices 4 and 5 (**Fig. 2d**) to move away from the nucleotide binding site, thereby
23 preventing full closure of the ATP lid. Moreover, the side-chain amino functional group of Lys112
24 forms a hydrogen bond with a benzoquinone oxygen of GA. This pocket configuration aligns with
25 the reduced cross-linking activity of the lysine pair mentioned above. Conversely, PU-H71 binds
26 deeply within the pocket. In this configuration, helices 4 and 5 are packed against helix 2 with
27 Lys112 and Lys58 in HSP90 α (or Lys107 and Lys53 in HSP90 β) positioned more favorably for
28 cross-linking. This arrangement of lysine residues is more likely to be found in the closed
29 conformation of HSP90 (**Fig. 2c**), as proposed by crystallographic studies (PDB: 2CG9)⁴⁹.

30 It is essential to reiterate that the cross-linking experiments were conducted to 'lock' HSP90
31 conformations with covalent bonds before resin-based affinity purification experiments using the
32 PU- or GA-beads. Consequently, the X-ray structures of PU- or GA-bound HSP90 NTD closely
33 reflect a preferred pocket configuration that each ligand may capture in the cell, and in this case,
34 for PU-H71, it is indicative of the pocket configuration of HSP90 in the epichaperomes.

35 Furthermore, differences in HSP90 conformation were corroborated by cross-linked pairs located
36 at the interfaces between NTD/MT (HSP90 α : Lys293-Lys363) and MD/CTD (HSP90 α : Lys444-
37 Lys616; HSP90 β : Lys435-Lys607) (**Fig. 2b**). These interfaces undergo significant reorientation
38 during the HSP90 conformational cycle, implying a distinct HSP90 conformation favored by PU-
39 H71 compared to GA. Lys444 in HSP90 α (Lys435 in HSP90 β) and Lys616 in HSP90 α (Lys607
40 in HSP90 β) are positioned either within the middle of the MD or in proximity to the central axis of
41 the HSP90 homodimer (**Fig. 2c**). The distance between these lysine residues can provide insights
42 into the relative placement of the monomer arms in specific HSP90 conformations (e.g., 20 Å in
43 closed-like conformations; 29 Å in open-like conformations). The lower cross-linking percentage
44 observed for Lys444 and Lys616 in HSP90 α (Lys435 and Lys607 in HSP90 β) in GA-favored
45 HSP90 suggests a longer distance (29 Å) between them, supporting GA's preference for binding
46 to an open-like conformation. In contrast, the moderate cross-linking percentage detected for

1 these residues in PU-H71-favored HSP90 implies a medium distance (20 Å) between them,
2 favoring a closed-like conformation enriched in epichaperomes (**Fig. 2c**).

3 Additionally, a third pair of cross-linked residues (Lys293 and Lys363 in HSP90 α) supports this
4 notion. Located near the interface between the NTD and the MD, their positions are sensitive to
5 the ligand binding state of the NTD, leading to changes in the relative positioning of secondary
6 structures near the NTD/MD interface and altering the distance between Lys293 α and Lys363 α .
7 Consistent with the cross-linked pair at MD/CTD interface, a closed-like conformation (16 Å) in
8 PU-H71 bound HSP90 will be more amenable than an open-like conformation (13 Å) in GA-bound
9 since the short distance might have limited the location of side-chains for cross-linking reactions.

10 In summary, our CX-MS data, supported by several cross-linked residue pairs situated in
11 structurally distinct regions, the nucleotide-binding pocket, and the NTD/MD and MD/CTD
12 interfaces, shed light on the conformation adopted by HSP90 within epichaperomes. These
13 findings underscore the notion that an enrichment of the closed-like conformation of HSP90 in
14 specific cellular environments favors the formation of epichaperomes.

15 **Specific PTMs support HSP90 incorporation into epichaperomes**

16 To uncover the factors that facilitate the enrichment of the epichaperome-favoring HSP90
17 conformation, we conducted a comprehensive examination of the HSP90 pools isolated by PU-
18 H71 and GA, searching for potential differences. Notably, we identified several peptides
19 phosphorylated on Ser231 and Ser263 in HSP90 α (Ser226 and Ser255 in HSP90 β) exclusively
20 in the PU-H71 cargo from ESCs (**Fig. 3a,b and Supplementary Data 3**). High-quality MS/MS
21 spectra (illustrated for Ser226 and Ser255 phosphopeptides in HSP90 β , **Fig. 3b**) coupled with
22 precise mass accuracy allowed for the unequivocal identification of the peptide sequences and
23 the phosphorylation sites. In contrast, these phosphorylated peptides were notably absent in
24 substantial quantities in the GA cargo (**Supplementary Data 3**).

25 Subsequently, we performed label-free quantitation of these phosphopeptides using ion intensity
26 measurements and observed a significant enrichment in the PU-beads cargo, particularly in the
27 case of Ser255 of HSP90 β . For instance, the Ser255 phosphopeptide displayed a nearly three-
28 fold enrichment in the PU-H71 cargo compared to the lysate, after protein loading normalization
29 using a representative tryptic peptide (**Fig. 3c**).

30 To gain further insights, we leveraged previously reported MS datasets of PU-H71-isolated cargo
31 from epichaperome-positive cancer cells^{13,19}, including MDA-MB-468 (triple negative breast
32 cancer), Daudi (Burkitt's lymphoma), IBL-1 (AIDS-related immunoblastic lymphoma), and NCI-
33 H1975 (non-small cell lung carcinoma), as well as from non-transformed (NT) proliferating cells
34 in culture (e.g., MRC5, lung fibroblast and HMEC, mammary epithelial cells). This analysis
35 revealed that phosphorylation of these serine residues is also enriched in cancer cells when
36 compared to NT cells (Ca:NT S255 = 16; S226 = 8; S263 = 12, **Fig. 3d**) establishing it as a
37 hallmark of both ESC and cancer epichaperomes. This observation further supports the idea of a
38 shared structural and architectural foundation for epichaperomes among ESCs and cancer cells.

39 As HSP90 is found alongside HSC70 in epichaperomes, we conducted an additional confirmatory
40 experiment. Here, we used YK5-B, a biotinylated probe that binds to HSC70 in epichaperomes,
41 and thus captures HSP90 in epichaperomes via HSC70¹⁹. PU-H71 and YK5-B were used to
42 isolate cargo from epichaperome-positive cancer cells, including MDA-MB-468 and OCI-Ly1
43 (breast cancer and diffuse large B-cell lymphoma, respectively), as well as from CCD-18Co colon
44 cells in culture (i.e., non-transformed proliferating cells in culture). We found that the Ser255 and
45 S226 phosphopeptides of HSP90 β were nearly four to five times more abundant in epichaperome-

1 positive cancer cells compared to non-transformed proliferating cells in culture, for both the PU-
2 cargo and the YK5-B cargo. Similar enrichment was noted for Ser263 and Ser231 in HSP90 α
3 (**Fig. 3e**). This analysis, thus, using both PU-H71 and YK5-B probes across diverse cell types,
4 underscores the robustness of our observations and reinforces the role of phosphorylation in the
5 acidic linker in shaping HSP90 within epichaperomes.

6 In light of these findings, made with two distinct probes and observed in ESCs, five cancer cell
7 lines, each representative of a distinct cancer type, and of three non-transformed, but proliferating,
8 cells in culture, it is evident that the epichaperome-specific agents target a subpopulation of
9 HSP90 characterized by high phosphorylation levels in the acidic linker between the NTD and the
10 MD, and this subpopulation predominantly assumes a closed-like conformation. In conjunction
11 with PU's preference for HSP90 within epichaperomes, and substantiated by YK5-B, a probe that
12 binds epichaperomes via HSC70, these results strongly indicate that phosphorylation at these
13 two serine residues is a key driver for HSP90 incorporation into epichaperomes and,
14 consequently, for epichaperome formation.

15 **Specific PTMs drive epichaperome formation and function**

16 To explore whether the phosphorylation of these serine residues plays a pivotal role in driving,
17 rather than merely resulting from, epichaperome formation, we next studied the phosphomimetic
18 (HSP90 β ^{S226E,S255E}) and the non-phosphorylatable (HSP90^{S226A,S255A}) mutants.

19 Notably, these serine residues are located within an intrinsically disordered region (IDR) of HSP90
20 (**Supplementary Fig. 5**). IDRs are pivotal elements in the intricate network of protein-protein
21 interactions (PPIs). These regions lack a fixed three-dimensional structure, granting them
22 exceptional flexibility. This structural adaptability enables proteins containing IDRs to assume
23 various conformations in response to specific cellular contexts or binding partners. Such
24 adaptability plays a crucial role in facilitating context-dependent involvement in distinct PPIs. In
25 the case of HSP90, these serine residues within the IDR may alter the dynamics and structure of
26 the charged linker, contributing to stabilizing the epichaperome-enabling conformation of this
27 chaperone, and in turn facilitating epichaperome formation.

28 To explore this hypothesis, we conducted computational analyses to investigate the impact of
29 each mutation on the flexibility of the charged linker (**Fig. 4a-c**). We constructed a model of the
30 putative epichaperome core - namely the ~300 kDa assembly, see **Fig.1** - based on the cryo-EM
31 structure of a multimeric HSP90 assembly (PDB: 7KW7). This structure represented 2xHSP90 α ,
32 protomer A and B, bound to 2xHSP70 and 1xHOP. To create the model, we substituted HSP90
33 with human HSP90 β using the closed-state cryo-EM structure (PDB: 8EOB). Additionally, we
34 computationally inserted the charged linker, which was missing in the cryo-EM structures (**Fig.**
35 **4a**).

36 We conducted all-atom molecular dynamics simulation of this pentameric protein assembly, with
37 each system containing all the components along with either the EE, AA, or WT HSP90 – in both
38 protomers. These simulations are intended to qualitatively explore the immediate response of the
39 assembly to the perturbation induced by mutations and not to provide an extensive
40 characterization of the assemblies' dynamics. By using a comparative MD-based approach we
41 explore how short-term changes in the structural dynamics of different components within a large
42 assembly may influence the emergence of states relevant for assembly stabilization. The
43 underlying premise is that nanosecond timescale residue fluctuations in regions specifically
44 responsive to certain states may facilitate large-scale rearrangements that underlie functional
45 changes.

1 These simulations revealed that the structure and conformation of the charged linker were
2 sensitive to the phosphorylation of the serine residues. In the pentameric assembly containing
3 the phosphomimetic EE mutant (i.e., HSP90^{S226E/S255E}), the linker of HSP90, protomer A, had a
4 high probability of forming a β -strand bordering the Ser226Glu residue (2.1% of β -strand A). This
5 strand remained stable over the duration of the simulation. This β -strand's formation significantly
6 decreased in the pentameric assembly containing the wild-type (WT, i.e., HSP90^{S226/S255}) protein
7 (0.4% of β -strand A), with no secondary structure element found in the assembly containing the
8 AA (i.e., HSP90^{S226A/S255A}) mutant (**Fig. 4b**). Notably, ATP binding, but not ADP binding, favored
9 a charged linker with a high content of β -strand A formation (2.1% vs. 0.3%, respectively, in the
10 EE mutant) (**Fig. 4b** and **Supplementary Fig. 6a**). This finding emphasizes that the observed
11 changes in the EE mutant were not merely due to the addition of charged residues; they were
12 intricately tied to the phosphorylation status and the specific context, including the nucleotide
13 environment permissive of the specific HSP90 conformation (i.e., closed-like). Intriguingly, the
14 strategic formation of β -strand A not only stabilized the charged linker but also induced a
15 conformational switch, flipping it into an 'up' conformation, thereby fully exposing the middle
16 domain of HSP90, where HSP70 binds (**Fig. 4c**, see HSP90 protomer A – HSP70 interface).
17 While other stabilized structural elements were observed in the analyzed assemblies containing
18 either the WT or the mutant HSP90s, no other had a similar conformational effect on the charged
19 linker as we observed for the β -strand A (see the effect of α -helices 1 through 6 in **Supplementary**
20 **Fig. 6a,b**).

21 We conducted dynamical residue cross-correlation analyses to explore how different protein units
22 or subdomains in the pentameric 2xHSP90-2xHSP70-HOP assemblies, featuring either the WT
23 (HSP90^{S226/S255}) or mutant (HSP90^{S226E/S255E} or HSP90^{S226A/S255A}) HSP90s, correlate in their
24 motions throughout the simulation (**Fig. 5a,b**). This analysis aimed to reveal how individual
25 components move in relation to each other. Positive dynamical cross-correlations spanning
26 different components of the assembly within the large epichaperome core may indicate enhanced
27 cooperative motions, suggesting increased interactions that contribute to the stability of the
28 assembled structure. Previous studies have employed similar analyses to investigate how ligand-
29 induced modulations influence the overall flexibility of HSP90 assemblies, facilitating progress
30 along the chaperone cycle, thereby supporting feasibility of this approach⁵⁰.

31 Indeed, we observed the highest correlation among the components in assemblies containing the
32 HSP90 EE phosphomimetic, mimicking the case where the charged linker is phosphorylated,
33 followed by the WT, and then the non-phosphorylatable HSP90 AA mutant (**Fig. 5a**). Notably, the
34 coordinated movements observed in the assemblies containing the HSP90 phosphomimetic
35 strongly support the idea that the HSP70-HSP90-HSP90-HSP70 or HSP70-HSP90-HSP90-
36 HSP70-HOP assemblies can be preferentially stabilized when the HSP90 charged linker is
37 phosphorylated (**Fig. 5b**). This observation aligns with the prominent ~300kDa band observed for
38 the epichaperome core in native PAGE (see **Fig. 1** showing HSP90 assemblies favored by PU-
39 H71).

40 In contrast, in the WT HSP90 assembly, coordinated movements were primarily observed
41 between the two HSP90 protomers, within HSP90, and between HSP90 and HSP70 and HOP,
42 specifically through HSP90 protomer B (**Fig. 5a,b**). These movements are more consistent and
43 favorable in the context of HSP90-HSP90-HSP70 or HSP90-HSP90-HOP assemblies. This
44 observation implies that the major, broad ~242 kDa band detected by the HSP90 antibody –
45 representing the primary HSP90-containing assembly observed in differentiated ESCs (**Fig. 1**)
46 and in non-transformed cells^{13-15,17,20} – may consist of such assemblies, along with HSP90 homo-
47 oligomers.

1 In summary, both MS evidence and computational models converge to support the conclusion
2 that phosphorylation of the charged linker is a crucial contributor to epichaperome assembly,
3 emphasizing its role in shaping not only HSP90, but also the stability and dynamics of the
4 epichaperome structure.

5 Next, we carried out an extensive biochemical and functional analysis to reinforce these findings.
6 Given the well-established tight association between HSP90 and other chaperones and co-
7 chaperones in epichaperomes^{13,19,20,51}, our focus shifted to a comprehensive evaluation of
8 chaperone and co-chaperone proteins co-purified with the phosphomimetic (HSP90 β ^{S226E,S255E})
9 and non-phosphorylatable (HSP90^{S226A,S255A}) mutants. Our strategy involved the purification of
10 protein complexes containing N-terminally mCherry-tagged HSP90 β in ESCs while retaining the
11 endogenous WT HSP90 proteins. Distinctly labeled ESCs (i.e., labeled with heavy or light isotope
12 lysine and arginine) expressing either the phosphomimetic or non-phosphorylatable mutant were
13 subjected to immunoprecipitation (IP), followed by SDS-PAGE separation and quantitative
14 analysis via MS to determine protein abundance (**Fig. 6a-c; Supplementary Data 4**). It is worth
15 noting that we performed IP separately for the phosphomimetic and non-phosphorylatable
16 mutants to minimize subunit exchange during IP⁵², thereby enhancing our ability to detect
17 changes in co-chaperone binding more accurately than previous studies⁵³.

18 We found co-chaperones were among the most abundant copurifying proteins, and most co-
19 chaperones reported to participate in epichaperome formation^{13,19} displayed prominent changes
20 in the phosphomimetic mutant (**Fig. 6b,c**). The increased presence of epichaperome-specific co-
21 chaperones (such as AHA1 and FKBP4)¹³ in phosphomimetic complexes compared to non-
22 phosphorylatable complexes highlights a stronger association with Ser226^P/Ser255^P HSP90 as
23 opposed to the non-phosphorylatable protein. However, we observed a slight reduction in the
24 levels of HSC70 and HOP within phosphomimetic complexes. This decrease is potentially
25 associated with specific subpopulations of HSP90 complexes that become more prevalent when
26 the non-phosphorylatable Ala mutant is overexpressed in cells. The introduction of two Ala
27 residues in the unstructured linker region of HSP90 may prompt the recruitment of HSC70 and
28 HOP, chaperones recognized for their ability to bind unstructured unfolded protein stretches⁵⁴. It
29 is important to note that these assemblies are distinct from epichaperomes. Due to the anti-
30 mCherry antibody capturing the entirety of the tagged HSP90, differentiation between specifically
31 epichaperome-related HSP90 and a mixture of epichaperomes and other pools becomes
32 challenging.

33 To address these limitations, we adopted a multi-pronged approach. Firstly, we utilized
34 immunoblotting with native cognate antibodies for chaperone assemblies retained on native
35 PAGE, coupled with chemical blotting using PU-probes. Additionally, we employed affinity capture
36 with PU-probes to quantify the amount of epichaperome components under each condition (**Fig.**
37 **7a**). For these experiments, we transfected cells with the phosphomimetic (HSP90 β ^{S226E,S255E}, EE
38 mutant) and with the non-phosphorylatable (HSP90^{S226A,S255A}, AA mutant) mutants, as well as with
39 HSP90 β WT or mCherry-tag only for control purposes. In this study, we chose human embryonic
40 HEK293 cells as our cell model since they exhibit intermediate epichaperome expression levels
41 (i.e., medium expressor, **Supplementary Fig. 7**), making them suitable for studying
42 epichaperome dependence. We confirmed comparable transfection efficiency for each construct,
43 with the tagged HSP90 β protein expressed in addition to the endogenous HSP90 β (**Fig. 7b**).

44 Our findings revealed that cells expressing the EE mutant exhibited higher levels of
45 epichaperomes compared to those expressing the AA mutant, as evidenced by immunoblotting
46 of various epichaperome components (including HSP90 α , HSC70, CDC37, AHA1, HOP, and
47 HSP110) (**Fig. 7c**, native PAGE) and chemical blotting with the PU-Cy5 epichaperome probe

1 (Fig. 7d). Notably, there was no significant change in the overall concentration of these proteins
2 in association with their incorporation into epichaperomes (Fig. 7c, SDS PAGE). Epichaperome
3 isolation using PU-beads as an affinity purification probe also revealed significantly greater
4 incorporation of chaperones, including mCherry-HSP90 β , and co-chaperones into
5 epichaperomes in cells expressing the EE mutant compared to those containing the AA mutant
6 HSP90 (Fig. 7e), with no substantial alterations observed in cells containing the control vectors
7 (Supplementary Fig. 8a). In contrast, overexpression of wild-type HSP90 in HEK293 cells had a
8 minimal impact on endogenous epichaperomes (Fig. 7c, native PAGE, and Supplementary Fig.
9 8a, PU-beads capture). This observation aligns with previous reports¹³ suggesting that factors
10 beyond chaperone concentration play a pivotal role in driving HSP90 incorporation into
11 epichaperomes. Notably, cargo isolated on the control probe (control beads, Supplementary Fig.
12 8b) showed no detection of HSP90.

13 We further established the dependency of epichaperome function, beyond its formation, on the
14 phosphorylation of HSP90 serine residues (Fig. 8,9). A key characteristic shared among high
15 epichaperome-expressing cells in PSC, CSC, and cancer cells is the hyperactivity of the
16 transcription factor c-MYC^{13,25-27}. In cancer, c-MYC is frequently overexpressed or mutated,
17 resulting in sustained activation, which drives uncontrolled cell proliferation⁵⁵. In ESCs, c-MYC
18 plays a crucial role in maintaining pluripotency and self-renewal, crucial for preserving the
19 undifferentiated state of ESCs⁵⁶. We therefore investigated the impact of HSP90 β
20 Ser226^P/Ser255^P on cellular behaviors such as self-renewal and proliferation.

21 To assess proliferation, ESCs were transfected with plasmids containing either the
22 phosphomimetic (HSP90 β ^{S226E,S255E}) or non-phosphorylatable (HSP90 β ^{S226A,S255A}) mutant.
23 Notably, ESCs transfected with the HSP90 β phosphomimetic mutant displayed a significantly
24 higher proliferative rate ($P < 0.0001$, $> 25\%$) compared to those transfected with the non-
25 phosphorylatable variant, regardless of whether medium (1x) or high (2x) plasmid concentrations
26 were employed (Fig. 8a). This observation lends support to the notion that HSP90 β
27 Ser226^P/Ser255^P, and consequently, epichaperomes, play a crucial role in ESC proliferation.

28 Differentiation of ESCs results in a decreased proliferative rate, as indicated by the doubling time
29 of ZHBTc4 ES cells (~12 h) and trophoblast-differentiated cells (~25 h)³². Since differentiation is
30 also closely associated with the disassembly of epichaperomes, we next examined the
31 phosphorylation levels of HSP90 β at Ser226 and Ser255 in cells with varying self-renewal
32 capacities. We utilized the TET-repressible *oct4* mouse ESC line ZHBTc4, where the Oct4
33 expression is suppressed in the presence of doxycycline for ESC differentiation into trophoblast-
34 like cells (Troph)³¹. In this experiment, we expressed WT mCherry-HSP90 β in ZHBTc4 cells and
35 quantified phosphopeptides in both ESCs and trophoblast cells following ESC differentiation (Fig.
36 8b, Supplementary Data 5). After normalizing the data to mCherry-HSP90 β protein loading
37 (middle panel, ES/Troph = 0.44), we observed a 30% higher phosphorylation of HSP90 β at
38 Ser255 in stem cells compared to differentiated cells (left panel, ES/Troph = 0.57).
39 Phosphorylation levels of HSP90 β at Ser226 appeared to remain unchanged under these
40 experimental conditions after normalizing to protein loading (right panel, ES/Troph = 0.45).

41 Pluripotency hinges on crucial transcription factors like Oct4. Oct4 is widely recognized as one of
42 the principal transcription factors governing the self-renewal of both pluripotent stem cells and
43 cancer cells⁵⁷. We find Oct4 interacts with epichaperomes in ESCs (Supplementary Data 1) and
44 exhibits significant enrichment in the cargo captured with the Ser226/Ser255 phosphomimetic
45 compared to the non-phosphorylatable HSP90 (Supplementary Data 4, Fig. 8c, 1.4-fold EE :
46 AA). To validate the reliance of Oct4 on epichaperomes, we examined Oct4 levels in both MDA-
47 MB-468 cancer cells and HEK293 cells transfected with the various HSP90 plasmids. Additionally,

1 we utilized affinity capture with PU-probes (**Fig. 8d-f** and **Supplementary Fig.8a**). Notably, we
2 observed that cells expressing the phosphomimetic EE mutant showed significantly elevated
3 levels of Oct4, both overall (**Fig. 8e**) and within epichaperomes (i.e., those sequestered within the
4 epichaperomes, **Fig. 8f**), compared to cells expressing the HSP90 AA mutant. No detectable
5 differences were observed under control conditions (WT HSP90 and empty vector only)
6 (**Supplementary Fig. 8a**). Additionally, Oct4 was sequestered by epichaperomes in MDA-MB-
7 468 cells, supporting the idea that epichaperomes play a role in regulating pluripotency through
8 both direct and indirect regulation of Oct4.

9 Epichaperomes play a pivotal role in supporting enhanced proliferation by altering the regulation
10 of various proteins involved in cell signaling^{3,13,19}. Higher epichaperome levels translate to a
11 greater number of proteins being affected, resulting in increased signaling output^{13,17,58}. We
12 therefore next assessed the signaling output of cells transfected with the various HSP90 mutants.
13 We observed a significantly heightened epichaperome-dependent impact on key signaling
14 effector proteins involved in cell growth and proliferation (i.e., MEK, AKT, and mTOR) in cells
15 expressing the HSP90 EE mutant compared to those expressing the AA mutant. This was evident
16 in both the increased phosphorylation status of these effector proteins (**Fig. 9a,b**) and their
17 enhanced recruitment to epichaperome platforms (**Supplementary Fig. 9a-c**) in cells expressing
18 the EE mutant, as compared to those expressing the AA mutant. Importantly, these effects
19 occurred without notable changes in the expression levels of the proteins (**Supplementary Fig.**
20 **9a, b**). No measurable differences were observed under control conditions (WT HSP90 and empty
21 vector only) (**Fig. 9b and Supplementary Fig. 9a, b**).

22 Epichaperome formation fuels aggressive behaviors in cells^{51,59}. Indeed, when observed under a
23 microscope, we noted that, in comparison to cells expressing the non-phosphorylatable AA
24 mutant (HSP90 β ^{S226A,S255A}), those expressing the phosphomimetic EE mutant (HSP90 β ^{S226E,S255E})
25 displayed a higher prevalence of cells with an elongated phenotype and several protrusions (**Fig.**
26 **9a,b**), supportive of a mesenchymal-like phenotype⁶⁰. These morphological changes suggest a
27 shift towards a more stem cell-like state, or a more aggressive phenotype in the context of cancer,
28 in cells harboring the EE HSP90 mutant (i.e., with a high epichaperome load), a feature not
29 observed in cells carrying the AA HSP90 mutant (i.e., not permissive of epichaperome formation).

30 Previous studies have found that irrespective of the tumor type, 60-70% of tumors contain HSP90-
31 HSC70 epichaperomes^{13,19}. Additionally, epichaperomes are known to specifically form in
32 diseased tissue³. To assess whether our observations regarding the impact of the HSP90 charged
33 linker, derived from cell models, extend to human patients and are not artifacts specific to cultured
34 cells, we obtained surgical specimens from breast and pancreatic cancer surgeries (n = 18 tissues
35 from 9 patients, **Fig. 10a-d**). Both tumor (n = 9) and tumor adjacent (n = 9) tissues, determined
36 by gross pathological evaluation to be potentially non-cancerous, were analyzed for
37 epichaperome levels using Native PAGE. Additionally, total HSP90 β and phosphorylated HSP90 β
38 at Ser226 were assessed by SDS PAGE and immunoblotting with specific antibodies. To mitigate
39 potential biases arising from varying HSP90 levels, each pair was normalized based on HSP90
40 concentration. Despite challenges in obtaining high-quality epichaperome profiles from surgical
41 samples, a robust correlation emerged between epichaperome expression and Ser226
42 phosphorylation (**Fig. 10c,d**). Tissues positive for epichaperomes exhibited p-Ser226 HSP90 β
43 positivity, and conversely, those negative for epichaperomes showed no or negligible p-Ser226
44 signal.

45 Collectively, these multifaceted biochemical and functional lines of evidence establish a
46 compelling connection between structural features in HSP90 and the processes of epichaperome
47 formation and function. These findings lend robust support to the hypothesis that the regulation
48 of epichaperome processes in ESC and cancer cells—encompassing critical factors such as

1 proliferative potential, self-renewal capacity, plasticity, and signaling output—crucially relies on
2 the specific phosphorylation events taking place at key residues within HSP90's charged linker.

3 **DISCUSSION**

4 The intricate network of protein-chaperone interactions within cells plays a critical role in
5 maintaining protein homeostasis and cellular function. In recent years, the discovery of
6 epichaperomes as specialized chaperone complexes in both cancer cells and pluripotent stem
7 cells has opened new avenues for understanding chaperone biology. This investigation offers
8 valuable insights into the structural and regulatory intricacies of epichaperomes, with particular
9 attention to the pivotal role played by PTMs of HSP90 in orchestrating their formation and function.

10 A central discovery in this investigation is the recognition of specific PTMs on HSP90, especially
11 at Ser226 and Ser255, as critical factors governing the assembly of epichaperomes. Our data
12 reveal that phosphorylation of these serine residues enhances the association of HSP90 with
13 other chaperones and co-chaperones, creating a microenvironment conducive to epichaperome
14 formation. This finding underscores the significance of PTMs in regulating chaperone assemblies
15 and highlights the potential of targeting these modifications for therapeutic intervention.

16 Chaperones appear to be highly susceptible to structural and functional regulation by a spectrum
17 of PTMs. For example, PTMs of HSP90 provide an important regulatory element, modulating co-
18 chaperone and client protein binding⁶¹⁻⁶⁵, ATPase activity⁶⁶, conformational cycle^{62,65-67}, turnover⁶⁸
19 and small molecule affinity^{12,38}. Similar to minor changes in primary sequence, these PTMs likely
20 regulate the access to and occupancy of key conformational states of HSP90 for in vivo
21 processing of some essential clients. Our investigation pinpoints crucial PTMs that remodel the
22 functional profile of HSP90, metamorphosing it from a protein-folding entity into epichaperomes,
23 a platform orchestrating the reorganization of PPI networks for heightened cellular adaptability
24 and proliferation.

25 Our study uncovered a fascinating aspect of PTMs in HSP90 within epichaperomes –
26 phosphorylation events occur in an IDR of the protein. The strategic placement of these PTMs in
27 the IDR holds profound significance, suggesting that they influence HSP90's conformation and
28 function beyond the traditional structured regions. This adaptability is crucial for HSP90's
29 participation in distinct PPIs, allowing it to stabilize the epichaperome-enabling conformation and
30 restructure the interactions of numerous proteins in response to cellular stressors. Intriguingly,
31 previous studies in yeast⁶⁹, where the IDR was substituted with glycine-glycine-serine residues,
32 align with our findings. These studies suggested that the charged linker (encompassing the IDR),
33 influenced by the N-domain of HSP90, can adopt a structured form. This structured form, in turn,
34 can stabilize interactions between specific HSP90 domains, influencing HSP90 dynamics, co-
35 chaperone binding, and overall biological function, especially in conditions of cellular stress.

36 Changes in PPI networks play a fundamental role in cellular responses to stressors and the
37 coordination of various biological processes¹⁸. These alterations, often induced by external
38 stressors, are vital for the cell's ability to adapt and function under different conditions. Notably,
39 less than 10% of human PPIs remain unaffected by stress-induced perturbations, highlighting the
40 widespread impact of cellular stress on the interactome. These changes, influenced by factors
41 such as PTMs and protein conformation, are essential for species-specific adaptation and
42 contribute to PPI network malfunctions observed in diseases.

43 One intriguing question is which kinase could phosphorylate HSP90 at these serine residues? A
44 likely candidate is casein kinase II (CK2)^{70,71}. CK2 is sequestered to epichaperomes in ESCs and
45 in cancer cells¹³. Notably, CK2 is overexpressed in highly proliferative cells⁷² and plays a role in

1 phosphorylating numerous protein substrates involved in cell proliferation and survival⁷³.
2 Moreover, the mutation of CK2 has been shown to abolish the viability of both PSCs⁷⁴ and tumor
3 cells^{75,76}, indicating a potential direct link between epichaperome function and cellular physiology,
4 possibly mediated by CK2 phosphorylation, which remains to be confirmed.

5
6 The implications of our study go beyond providing structural and mechanistic insights. We present
7 compelling evidence that phosphorylation of HSP90 at Ser226 and Ser255 not only promotes
8 epichaperome formation but also influences cellular behaviors, including proliferation and self-
9 renewal. This suggests a direct link between epichaperome function and cellular physiology,
10 particularly crucial in contexts such as cancer and stem cell maintenance, where robust
11 proliferation and adaptation are vital.

12 Plasticity, a key characteristic associated with both ESCs and cancer cells⁷⁷, is also implicated in
13 our findings. The morphological changes observed in cells expressing the phosphomimetic
14 HSP90 mutant—specifically, the higher prevalence of cells with an elongated phenotype and
15 several protrusions—hint at a mesenchymal-like phenotype⁶⁰. This phenotypic shift is often
16 associated with increased plasticity and is indicative of a more stem cell-like state. Our findings
17 suggest a potential role for epichaperomes in modulating this dynamic process of cellular
18 transition between different phenotypic states.

19 The link between pluripotency and cancer is particularly intriguing. Cellular stress is increasingly
20 recognized as a pivotal factor that can shift the balance between cellular pluripotency and the
21 development of malignancies. The process of dedifferentiation, observed in regeneration in plants
22 and some vertebrates, involves the deactivation of genes responsible for cell-specific functions,
23 re-entry into the cell cycle, proliferation, and activation of pluripotency-associated genes⁷⁸.
24 Tumors also undergo dedifferentiation, where cancer cells revert to a less differentiated state, re-
25 express stem cell genes like Oct4, leading to the emergence of cancer stem-like cells with
26 enhanced metastatic potential and treatment evasion⁷⁹. Our study proposes epichaperomes as
27 significant mediators of changes in cellular identity, partly through Oct4.

28 The revelation of HSP90's dysfunctional multimeric states carries implications for therapeutic
29 interventions^{3,16}. Instead of universally inhibiting all HSP90 pools, a paradigm shift comes to the
30 fore with precision medicine strategies. The prospect of targeting specific pathologic
31 conformations while preserving normal HSP90 functions emerges as a promising direction. This
32 shift beckons researchers to navigate the intricate interplay of HSP90 conformations as they forge
33 ahead in the quest for innovative therapeutic approaches. Our study also confirms the notion that
34 small molecule HSP90 binders have distinct preference for HSP90 conformers in cells, reinforcing
35 the finding that not all HSP90 inhibitors act equally well or equally selectively on specific disease-
36 promoting HSP90 conformations or disease-associated HSP90 assemblies in comparison with
37 HSP90 conformers found in normal cells. The first feature determines drug efficacy, whereas the
38 latter influences the safety profile during administration.

39 In conclusion, our study unravels the intricate interplay between PTMs, conformational regulation,
40 and biological functions of HSP90 within epichaperomes. These findings have implications for the
41 development of novel therapeutic strategies targeting chaperone complexes in diseases
42 characterized by epichaperome dysregulation, such as in cancers and neurodegenerative
43 disorders. By deciphering the regulatory mechanisms underlying epichaperomes, we move one
44 step closer to harnessing their potential for precision medicine and therapeutic intervention.

45 **METHODS**

46 **Human biospecimens research ethical regulation statement**

1 Surgical specimens were obtained in accordance with the guidelines and approval of the
2 Institutional Review Board at Memorial Sloan Kettering Cancer Center, Biospecimen Research
3 Protocol# 09-121, project title: Ex-Vivo Testing of Breast Cancer Tumors for Sensitivity to
4 Inhibitors of Heat Shock Proteins and Signaling Pathway Inhibitors, S. Modi, PI, and Biospecimen
5 Research Protocol# Protocol# 09-121, project title: Ex-Vivo Testing of Breast Cancer Tumors for
6 Sensitivity to Inhibitors of Heat Shock Proteins and Signaling Pathway Inhibitors, S. Modi, PI, and
7 Biospecimen Research Protocol# 14-091, project title: Establishment and Characterization of
8 Unique Mouse Models Using Patient-Derived Xenografts . E. de Stanchina, PI. The source of
9 samples consists of unused portions of surgical specimens that are taken for reasons other than
10 research (i.e., for patients undergoing the procedures for medical reasons unrelated to need for
11 research samples or to the nature of the research). No individuals were excluded on the basis of
12 age, sex or ethnicity. Because breast cancer is a disease which overwhelmingly affects women,
13 and is a disease that is generally not seen in children, the vast majority of breast cancer patients
14 enrolled on protocol# 09-121 were females >18 years of age. Patient tissue samples were
15 obtained with consent provided in written form. Samples were de-identified before receipt for use
16 in the studies.

17

18 **Reagents and Chemical Synthesis**

19 All commercial chemicals and solvents were purchased from Sigma Aldrich or Fisher Scientific
20 and used without further purification. The identity and purity of each product was characterized
21 by MS, HPLC, TLC, and NMR. Purity of target compounds has been determined to be >95% by
22 LC/MS on a Waters Autopurification system with PDA, MicroMass ZQ and ELSD detector and a
23 reversed phase column (Waters X-Bridge C18, 4.6 x 150 mm, 5 µm) eluted with water/acetonitrile
24 gradients, containing 0.1% TFA. Stock solutions of all inhibitors were prepared in molecular
25 biology grade DMSO (Sigma Aldrich) at 1,000× concentrations. The PU-TCO, PU-CW800 and
26 YK5-B probes and relevant control probes, and the PU-beads and the control probes were
27 generated using published protocols^{13,19,35,80-85} or as described in **Supplementary Notes 1**. The
28 GA-biotin probe was purchased from Sigma (SML0985). Disuccinimidyl suberate (DSS) was
29 acquired from ThermoFisher (21655).

30 **Cell lines and culture conditions**

31 Cell line selection was not based on gender, sex or ethnicity. Cell lines were cultured according
32 to the providers' recommended culture conditions. Cells were authenticated using short tandem
33 repeat profiling and tested for mycoplasma. The breast cancer cell line MDA-MB-468 (HTB-132,
34 RRID: CVCL_0419), pancreatic cancer cell line ASPC1 (CRL-1682, RRID: CVCL_0152), non-
35 small cell lung cancer cell line NCI-H1975 (CRL-5908, RRID: CVCL_1511), B lymphoblast cell
36 line Daudi (CCL-213, RRID: CVCL_0008), lung fibroblast cells MRC5 (CCL-171,
37 RRID:CVCL_0440), the colon cell line CCD-18Co (CRL-1459, RRID: CVCL_2379) and the
38 Human Embryonic Kidney 293 (HEK293) cell line (CRL-1573, RRID: CVCL_0045) were
39 purchased from ATCC. IBL-1 (RRID:CVCL_9638) was derived from an AIDS-related
40 immunoblastic lymphoma⁸⁶. Mammary epithelial primary cells HMEC (PCS-600-010) were
41 purchased from Lonza. B-cell lymphoma cell line OCI-LY1 (RRID:CVCL_1879) was obtained from
42 the Ontario Cancer Institute. E14 mouse ES cells⁸⁷ were received as frozen ampules from TG
43 Fazio (U Mass Med School). Cells were feed-free and verified as of male mouse origin through
44 sequencing. ZHBTc4 mouse ES cells³¹ were received from D. Levasseur (U of Iowa). Cells were
45 cultured as ESCs without feeder cells in the absence of doxycycline. For hiPSC, healthy donor
46 fibroblasts purchased from Coriell were reprogrammed using CytoTune Sendai viruses³⁴.

47 **Mammalian cell culture and lysis**

48 Mouse feeder-free embryonic stem cells (E14 or ZHBTc4 line) were grown on tissue culture plates
49 coated with 0.2% gelatin. ESCs were cultured in Dulbecco's Modified Eagle Medium (DMEM;

1 Gibco 10829018) media supplemented with 10% fetal bovine serum (FBS, HyClone
2 SH30070.03HI), 2 mM L-glutamine, 0.1 mM nonessential amino acids (Gibco 11140050), 100 U
3 mL⁻¹ penicillin/streptomycin (Gibco 15140122), 0.1 mM beta-mercaptoethanol (Sigma M6250),
4 and 103 U mL⁻¹ leukemia inhibitory factor (LIF). Cells are grown in 37°C/5% CO₂ incubator with
5 media change every 2 days, passaged or harvested when 60-80% confluent. After harvesting,
6 cell pellets are washed with phosphate-buffered saline (PBS, GenClone 25-508) and flash frozen
7 before storing in -80°C. For pull-down and chemical cross-linking experiments, frozen cells are
8 thawed and lysed in Felts lysis buffer (20 mM HEPES pH 7.4, 50 mM KCl, 5 mM MgCl₂, 0.01%
9 NP-40) in the presence of protease inhibitors, phosphatase and deacetylase inhibitors.

10 **ESC and hiPSC differentiation**

11 ZHBTc4 cells were differentiated into trophoblasts through Oct4 repression. Cells were seeded
12 at a density of 2 × 10⁵ cells mL⁻¹ and grown in media with added doxycycline at a final
13 concentration of 200 ng mL⁻¹ for 96 h before harvest. E14 cells were spontaneously differentiated
14 using attached embryoid bodies (EB) culture. Briefly, cells were seeded at a density of 5 × 10⁴
15 cells/mL in sterile bacteriological petri dishes in differentiation media (ES media without LIF) and
16 cultured in 37°C/5% CO₂ incubator for 4 days to aggregate into EBs. When turned orange, media
17 were changed. On day 4, EBs were transferred into tissue culture dishes (without gelatin) at a
18 density of 100-200 EBs per 10 cm tissue culture dish. Attached EBs were cultured in differentiation
19 media in 37°C/5% CO₂ incubator for 14-18 days before harvest. hiPSC differentiated in midbrain
20 dopaminergic neurons were a gift from Dr. Lorenz Studer. Cells were differentiated into midbrain
21 dopamine neurons by a modified dual-SMAD inhibition protocol as described²⁰. hESCs were
22 dissociated into single cells using Accutase and plated at high density on Matrigel (BD). The cells
23 were subjected to timed exposure to LDN193189 (100 nM, Stemgent), SB431542 (10 μM, Tocris),
24 SHH C25II (100 ng mL⁻¹, R&D), Purmorphamine (2 μM, Stemgent), FGF8 (100 ng mL⁻¹, R&D)
25 and CHIR99021 (CHIR; 3 μM, Stemgent) to induce midbrain floor plate precursors. For mDA
26 neuron induction, floor plate precursors were maintained in mDA differentiation media containing
27 Neurobasal/B27/L-Glut (NB/B27; Invitrogen) supplemented with CHIR (until day 13) and with
28 BDNF (brain-derived neurotrophic factor, 20n mL⁻¹; R&D), ascorbic acid (0.2 mM, Sigma), GDNF
29 (glial cell line-derived neurotrophic factor, 20 ng mL⁻¹; R&D), TGFβ3 (transforming growth factor
30 type β3, 1 ng mL⁻¹; R&D), dibutyryl cAMP (0.5 mM; Sigma), and DAPT (10 μM; Tocris). On day
31 20, cells were dissociated using Accutase and replated on dishes pre-coated with polyornithine
32 (PO; 15 μg mL⁻¹)/laminin (1 μg mL⁻¹)/fibronectin (2 μg mL⁻¹) in differentiation medium
33 (NB/B27 + BDNF, ascorbic acid, GDNF, dbcAMP, TGFβ3 and DAPT). On day 30 of differentiation,
34 cells were dissociated using Accutase and replated on dishes pre-coated with polyornithine (PO;
35 15 μg mL⁻¹)/ laminin (1 μg mL⁻¹)/ fibronectin (2 μg mL⁻¹) in differentiation medium
36 (NB/B27 + BDNF, ascorbic acid, GDNF, dbcAMP, TGFβ3 and DAPT) supplemented with 10 μM
37 Y-27632 (until day 32). Two days after plating, cells were treated with 1 μg mL⁻¹ mitomycin C
38 (Tocris) for 1 h to kill any remaining proliferative contaminants. The mDA neurons were fed every
39 2 to 3 days and maintained without passaging until they were assayed at day 65. To prevent
40 neurons from lifting off, laminin and fibronectin were supplemented into the media every 7–10
41 days.

42 **Cell culture and transfections**

43 Monolayer cultures of MDA-MB-468 and HEK293 cells were grown in high glucose (4.5 g L⁻¹)
44 DMEM containing 10% FBS and 1× antibiotic and antimycotic (100×ABAM, GIBCO) in a 37°C
45 incubator supplied with 5% oxygen-air atmosphere. For native electrophoresis, and in-gel
46 fluorescence studies, 1 × 10⁷ cells were seeded in 100 mm dishes (Corning) at 70% confluency
47 in DMEM supplemented with 10% FBS and 1×ABAM. Next day, spent medium was changed with
48 fresh serum and antibiotic free DMEM for 1 h before performing transfections. Cells were
49 transfected using lipofectamine 3000 (Invitrogen) with 4 μg of mCherry empty vector, mCherry-

1 HSP90 β -Wild type (mCherry-HSP90 β -WT), mCherry-HSP90 β -S226A, S255A mutant (mCherry-
2 HSP90 β -AA) or mCherry-HSP90 β -S226E, S255E mutant (mCherry-HSP90 β -EE) plasmids. See
3 Supplementary Note 2 for plasmid sequences. Transfection mixtures were prepared in OptiMEM
4 (Gibco). Post 6 h of transfection, medium was changed with 10% FBS and 1 \times ABAM
5 supplemented DMEM. Cells were harvested in native lysis buffer for future analyses.

6 **Primary specimen processing**

7 Frozen tumor and matched tumor adjacent tissues were cut into small pieces using surgical
8 blades and weighed using a precision balance. 74 mg of tissue was homogenized in 200 μ L of
9 1 \times native lysis buffer in 1.5 mL microtube homogenizer for each sample. Homogenization was
10 performed on dry ice. Post homogenization samples were incubated on ice for 30 min followed
11 by centrifugation at 12,000 \times g at 4 $^{\circ}$ C for 15 min. Supernatant was collected, and protein
12 quantification was done using BCA method. Samples were normalized using total HSP90 β levels
13 for each tissue pairs. An initial SDS-PAGE was run using 5 μ g of total protein for each sample.
14 Total protein loads were adjusted to ensure equal levels of total HSP90 β in tumor and
15 corresponding matched adjacent tissue. Samples were then processed for native PAGE and
16 SDS-PAGE to check for HSP90 β and p-Ser226 HSP90 β as described below.

17 **Native gel electrophoresis and western blot**

18 Native gel electrophoresis was performed as reported⁸⁸. Namely, 1 \times 10⁷ cells were lysed in 20
19 mM Tris pH 7.4, 20 mM KCl, 5 mM MgCl₂, 0.01% NP40, and 10% glycerol buffer containing
20 protease and phosphatase inhibitors (native lysis buffer), by a freeze-thaw procedure. Protein
21 concentrations were measured by using the BCA assay according to the manufacturer's protocol
22 (Pierce™ BCA Protein Assay Kit, Thermofisher Scientific, Waltham, MA). One hundred
23 micrograms (100 μ g) of protein were loaded in 4 to 10% native gel and run using native 1 \times Tris-
24 Glycine buffer (25 mM Tris, 192 mM glycine) at 4 $^{\circ}$ C in a cold room at 125V. Following
25 electrophoresis, proteins were transferred to PVDF membrane, by wet transfer (25 mM Tris, 192
26 mM glycine, 20% (v/v) methanol, 0.02% SDS) at 100V in the cold room. Membranes were then
27 blocked for 1 h in 5% BSA in TBS/0.1% Tween 20. The blots were then probed with the following
28 antibodies: HSP90 β (SMC-107; RRID:AB_854214; 1:2,000) and HSP110 (SPC-195;
29 RRID:AB_2119373; 1:1,000) from Stressmarq; HSC70 (SPA-815; RRID:AB_10617277; 1:1,000),
30 and HOP (SRA-1500; RRID:AB_10618972; 1:1,000) from Enzo; HSP90 α (ab2928;
31 RRID:AB_303423; 1:6,000), AHA1 (ab56721, RRID:AB_2273725, 1:1000) from Abcam; CDC37
32 (4793; RRID:AB_10695539; 1:1,000), HOP (5670; RRID:AB_10828378; 1:1,000), from Cell
33 Signaling Technologies. The blots were washed with TBS/0.1% Tween 20 and incubated with
34 appropriate HRP-conjugated secondary antibodies: goat anti-mouse (1030-05, RRID:
35 AB_2619742, 1:5,000), goat anti-rabbit (4010-05, RRID: AB_2632593, 1:5,000) and goat anti-rat
36 (3030-05, RRID: AB_2716837, 1:5,000) (Southern Biotech, Birmingham, AL, USA).] The
37 chemiluminescent signal was detected with Enhanced Chemiluminescence (ECL) reagent
38 according to manufacturer's instructions and visualized using Chemi Doc (Biorad) and analyzed
39 using Image Studio Lite Version 5.2. (LI-COR Biosciences). NativeMark unstained protein
40 standard (Invitrogen, LC0725) was used to estimate molecular weight of protein complexes in
41 native gel electrophoresis and Western blotting.

42 **SDS-PAGE and western blot**

43 Proteins were extracted in 20 mM Tris pH 7.4, 20 mM KCl, 5 mM MgCl₂, 0.01% NP40, and 10%
44 glycerol buffer containing protease and phosphatase inhibitors (native lysis buffer), by a freeze-
45 thaw procedure. Protein concentrations were measured by using the BCA assay according to the
46 manufacturer's protocol (Pierce™ BCA Protein Assay Kit, Thermofisher Scientific, Waltham, MA).
47 Ten to thirty micrograms (10 to 30 μ g) of total protein were subjected to SDS-PAGE, transferred
48 onto PVDF membrane, by wet transfer (Towbin buffer: 25 mM Tris, 192 mM glycine, 20% (v/v)

1 methanol) at 100V in cold room. Membranes were then blocked for 1 h in 5% BSA in TBS/0.1%
2 Tween 20 and incubated overnight with the indicated antibodies. HSP90 β (SMC-107;
3 RRID:AB_854214; 1:2,000) and HSP110 (SPC-195; RRID:AB_2119373; 1:1,000) from
4 Stressmarq; HSC70 (SPA-815; RRID:AB_10617277; 1:1,000), and HOP (SRA-1500;
5 RRID:AB_10618972; 1:1,000) from Enzo; HSP90 α (ab2928; RRID:AB_303423; 1:6,000), AHA1
6 (ab56721, RRID:AB_2273725, 1:1,000) from Abcam; p-MEK1/2 (S217/221) (9154;
7 RRID:AB_2138017; 1:1,000), MEK1/2 (9122; RRID:AB_823567; 1:1,000), p-mTOR (S2448)
8 (5536; RRID:AB_10691552; 1:500), mTOR (2983; RRID:AB_2105622; 1:1,000), CDC37 (4793;
9 RRID:AB_10695539; 1:1,000), HOP (5670; RRID:AB_10828378; 1:1,000), p-S6 ribosomal
10 protein (Ser235/236) (4858; RRID:AB_916156; 1:2,000), S6 ribosomal protein (2217;
11 RRID:AB_331355; 1:3,000), Oct4 (2840, RRID:AB_2167691, 1:2,000), p-AKT (S473) (9271,
12 RRID:AB_329825, 1:2000), AKT (4691, RRID:AB_915783, 1:3000), HSP70 (ADI-SPA-810,
13 RRID:AB_10616513, 1:2000) from Cell Signaling Technologies, β -actin (A1978, RRID:
14 AB_476692, 1:3000) from Sigma-Aldrich, and mCherry (PA5-34974, RRID:AB_2552323,
15 1:2,000) and p-Ser226 HSP90 β (PA5-105480, RRID:AB_2816908, 1:1,000) from Fisher
16 Scientific. The blots were washed with TBS/0.1% Tween 20 and incubated with appropriate HRP-
17 conjugated secondary antibodies: goat anti-mouse (1030-05, RRID: AB_2619742, 1:5,000), goat
18 anti-rabbit (4010-05, RRID: AB_2632593, 1:5,000) and goat anti-rat (3030-05, RRID:
19 AB_2716837, 1:5,000) (Southern Biotech, Birmingham, AL, USA). The chemiluminescent signal
20 was detected with ECL reagent according to manufacturer's instructions and visualized using
21 ChemiDoc MP imaging system (Biorad) and analyzed using Image Studio Lite Version 5.2. (LI-
22 COR Biosciences). Thermo Scientific PageRuler Plus prestained protein ladder (Fisher Scientific,
23 26619) or Precision Plus protein standards (Bio-Rad, 161-0375) were used as size standards in
24 protein electrophoresis and Western blotting.

25 **Coomassie and Ponceau S staining**

26 Where indicated, gels after native PAGE or SDS-PAGE were washed with deionized water three
27 times for 5 min and incubated with Coomassie G-250 stain (Bio-Rad) for 1 h. The gels were
28 washed with water after to remove the excess of the dye and imaged. Where indicated,
29 membranes after protein transfer were incubated with Ponceau S solution (Sigma) for 10 min,
30 then were washed with water to remove the excess of the dye and imaged.

31 **Primary specimen analyses**

32 Specimens were harvested as previously reported⁸⁹. Briefly, the surgical team delivered
33 specimens in tightly sealed, sterile, leak-proof bags without fixatives. This maintained specimens
34 in their fresh state, crucial for downstream analyses. Fresh specimens underwent sterile
35 harvesting by the pathologist or assistant, using laminar flow hoods. Harvesting times were
36 meticulously recorded, kept under 30 minutes post-surgery to mitigate cold ischemia effects.
37 Primary breast tumor specimens were selectively obtained from the index lesion's periphery,
38 avoiding central necrosis. Recognition criteria for necrotic tissue included color loss, softness,
39 and demarcation from viable tissue. Normal breast tissue samples (e.g., normal dense/fibrous
40 breast parenchyma) are taken from distant locations, at least 1 cm grossly away from the target
41 lesion if feasible. In contrast, due to the relatively small size of the pancreas and the nature of
42 surgical procedures, normal pancreas samples collected were typically in close proximity to the
43 tumor. Whipple procedures typically involve the resection of the head of the pancreas, while distal
44 procedures focus on the resection of the tail. Samples were initially stored in tubes with MEM and
45 antibiotics and transported on wet ice to the laboratory immediately after procurement. Upon
46 reaching the laboratory, samples were transferred to cryovials, 'snap' frozen, and stored at -80 °C
47 for future molecular analyses.

48 **Chemical blotting**

1 For in-gel blotting using PUTCO, cells were harvested in 20 mM Tris pH 7.4, 20 mM KCl, 5 mM
2 MgCl₂, 0.01% NP40, and 10% glycerol buffer containing protease and phosphatase inhibitors
3 (native lysis buffer), by a freeze-thaw procedure. Protein concentrations were measured by using
4 the BCA assay according to the manufacturer's protocol (Pierce™ BCA Protein Assay Kit,
5 ThermoFisher Scientific, Waltham, MA). One hundred micrograms (100 µg) of protein were
6 incubated with 1 µM of PUTCO in a total volume of 42 µL. Post 3 h of incubation samples were
7 loaded in 4 to 10% native gel and run using native 1× Tris-Glycine buffer at 4°C in cold room at
8 125V. Following electrophoresis, the gel was incubated in 30 mL of 700 nM Cy5-Tetrazine
9 containing ice cold 1× Tris-Glycine buffer at room temperature (RT) for 15 min for the click reaction
10 to occur. After 15 min, the gel was washed thrice (5 min each) with ice cold 1× Tris-Glycine buffer.
11 The gel was then imaged using ChemiDoc MP imaging system (Biorad). Alexa 546 channel
12 (illumination: Epi-green, 520–545 nm excitation, Filter: 577–613 nm filter for green-excitable
13 fluorophores and stains) was used to visualize mCherry-tagged species, and native page ladder
14 (NativeMark™ Unstained Protein Standard, Cat. No. LC0725, Invitrogen™). The Cy5 channel
15 (illumination: Epi-far red, 650–675 nm excitation, Filter: 700–730 nm filter for far red-excitable
16 fluorophores and stains) was used for imaging PUTCO staining. Post capturing, the images from
17 the two channels were merged to get the alignment of the bands with respect to the molecular
18 weight ladder in Image Lab 6.1 (Bio-Rad). For in cell blotting using PU-CW800, E14 cells were
19 plated at a seeding density of 1×10^6 per 10 cm plate and grown for 44 h before treatment with
20 either PU-CW800 or control fluorophore (SS27) at a concentration of 1 µM in culture media for 4
21 h while incubating at 37°C, 5% CO₂. Following the treatment, cells were harvested and lysed by
22 dounce homogenization in Felts lysis buffer (20 mM HEPES at pH 7.4, 50 mM KCl, 2 mM EDTA,
23 and 0.01% NP40) supplemented with protease, phosphatase, and deacetylase inhibitors. Cell
24 lysates were buffer exchanged with fresh Felts lysis buffer containing supplements to remove any
25 unbound drug before loading into a native gel. For visualization of PU-CW800 fluorescence and
26 total protein, 200 µg of cell lysate was loaded onto a 4-10% native gradient gel and resolved at
27 4°C for 5 h. Fluorescence was visualized on LI-COR Odyssey CLx using Image Studio™
28 Software (LI-COR Biosciences) and then total protein was visualized on the same gel using
29 Coomassie Brilliant Blue R250 stain. Band(s) with observable fluorescent signal were then
30 processed by in-gel digestion and analyzed for LC-MS/MS to identify major proteins.

31 **SILAC and ESC transfection**

32 For metabolic labeling with SILAC (stable-isotope labeling of amino acid in cell culture), ESCs
33 were cultured and passaged five times at 48 h intervals in media containing SILAC DMEM
34 (Thermo Fisher 88364) supplemented with 13C- and 15N-labeled heavy L-arginine (84 mg L⁻¹,
35 Cambridge isotope CNLM-539-H) and L-lysine (146 mg L⁻¹, Cambridge isotope CNLM-291-H) or
36 supplemented with 12C- and 14N-labeled light L-arginine (Fisher BP2505100) and L-lysine
37 (Fisher J6222522) amino acids for five passages to ensure complete stable isotope incorporation.
38 For heterologous expression of HSP90 AA or EE mutants, cells were then reverse transfected
39 with plasmid DNA using Lipofectamine™ 3000 Transfection Kit (Invitrogen #L3000015) and
40 incubated at 37°C, 5% CO₂ for 72 h at which point they were harvested.

41 **Measurement of cell proliferation**

42 E14 cells were transfected and incubated in 37°C/5% CO₂ incubator for 24 h. Cells were then
43 replated to 6-well plate at the same dilution factor for each transfection treatment condition and
44 then returned to incubator. At 60 h post-transfection, cell proliferation was determined via cell
45 count for all conditions.

46 **Confocal microscopy**

47 HEK293 cells transfected with mCherry-HSP90β-AA or mCherry-HSP90β-EE plasmids were
48 seeded at a density of 1.8×10^6 cells mL⁻¹ on coverslips in a monolayer in six well plates and then

1 grown overnight for the cells to attach. Cover slips were mounted with ProLong™ Gold antifade
2 mountant with DAPI. Imaging was done using Leica SP8 Stellaris microscope. Images were
3 analyzed using Image J and Leica LAS X lite software. Cell morphology was manually inspected,
4 and the percentage of cells exhibiting an elongated phenotype and several protrusions was
5 calculated. Specifically, cells transfected with mCherry were assessed, and those displaying the
6 described features were counted. The percentage was then determined based on the total
7 number of mCherry-transfected cells observed.

8 **Chemical precipitation and cross-linking**

9 The GA-affinity beads were prepared by incubating GA-biotin (Sigma SML0985) with Dynabeads
10 M-280 Streptavidin (ThermoFisher 11205D) at 4°C for 2.5 h. The GA-bound beads were then
11 incubated with cleared cell lysates or cross-linked cell lysates overnight at 4°C. For PU-beads
12 affinity capture, cell lysates were incubated with PU-beads or control beads at 4°C for 3.5 h.
13 Following incubation, bead conjugates were washed three times in lysis buffer before elution with
14 sample buffer. The chemical cross-linking and HSP90 purification experiments were carried out
15 in >3 replicates for both ligands. Samples were analyzed separately, and statistical significance
16 was assessed.

17 **Chemical precipitation and immunoblotting**

18 Cells were harvested in 20 mM Tris pH 7.4, 20 mM KCl, 5 mM MgCl₂, 0.01% NP40, and 10%
19 glycerol buffer containing protease and phosphatase inhibitors (native lysis buffer), by a freeze-
20 thaw procedure. Protein concentrations were measured by using the BCA assay according to the
21 manufacturer's protocol (Pierce™ BCA Protein Assay Kit, ThermoFisher Scientific, Waltham, MA).
22 PU-beads and control beads were washed with the native gel buffer 3 times prior use. Post
23 washing, 40 µL aliquots of the beads were distributed into the sample tubes. Five hundred
24 micrograms (500 µg) of total protein in 300 µL final volume, adjusted with native lysis buffer were
25 added. Samples were incubated for 3 h at 4°C on a rotor, followed by washing with native lysis
26 buffer four times. Post washing, 30 µL of 5× Laemmli buffer was added to the beads and boiled
27 at 95°C for 5 min. Ten micrograms (10 µg) of the lysates (2%) was used as input for the pull-down
28 experiment. Samples were then centrifuged at 13,000 × g for 20 min and supernatant collected
29 was loaded on to SDS-PAGE. The protein transfer and western blotting procedures were
30 performed as described in SDS-PAGE and western blot section.

31

32 **IUPred analysis for disorder prediction**

33 Sequence Preprocessing: The primary amino acid sequence of human HSP90β (P08238) and
34 HSP90α (P07900) were extracted in FASTA format. These sequences served as the input for
35 subsequent disorder prediction using the IUPred algorithm. Calculation of Disorder Scores: The
36 IUPred algorithm utilizes energy potentials derived from pairwise amino acid interactions to
37 assess the local structural propensities of each residue in the protein sequence. For each residue,
38 IUPred computes a disorder score within the range of 0 to 1. A score of 0 suggests a higher
39 likelihood of being ordered, while a score of 1 indicates a higher likelihood of being disordered.
40 Threshold for Disorder Classification: To classify residues as either ordered or disordered, a
41 threshold was applied to the calculated disorder scores. A common threshold of 0.5 was
42 employed, designating residues with scores above 0.5 as disordered. The output of the IUPred
43 analysis consisted of a disorder profile, providing disorder scores for each residue in the input
44 protein sequence. Residues were categorized based on the applied threshold, facilitating the
45 identification of regions with a high probability of disorder. All analyses were performed with the
46 default parameters of the IUPred algorithm. The results presented here are based on the specific
47 sequence input and the applied threshold for disorder classification.

48 **Computational analyses**

1 *Protein complex preparation and docking calculations:* The structure comprising HSP90 β -
2 HSP70(2)-HOP proteins was developed using the molecular comparative modeling technique,
3 employing Modeller v10.4, the Modeller Python script⁹⁰, and experimental template structures
4 (PDB codes: 7KW7, 8EOB)^{10,91}. The cryo-EM structure of human HSP90 β (8EOB) served as the
5 basis for obtaining coordinates for HSP90 β (protomers A and B) in the developing model. To
6 construct the assembly involving HSP70 and HOP, we utilized the sequences and atomic cryo-
7 EM structure from the HSP90-HSP70-HOP-GR (7KW7) template. As these structures lacked
8 certain residues, including those in the charged linker (Glu222 - Lys273), we incorporated them
9 as intrinsic loops during computational processing. The target sequence for each HSP90 β
10 protomer was extracted from Uniprot ID: P08238. After model generation, we selected the optimal
11 model based on the Discrete Optimized Protein Energy (DOPE) score. The final model included
12 full-length HSP90 (excluding a ten-residue N-terminal disordered segment). For HOP and HSP70,
13 we maintained the sequences provided in PDB:7KW7. The validated model, equipped with co-
14 crystal ligands on each HSP90 β protomer, was imported into Maestro v13.3 (Schrodinger LLC,
15 2022-3). Mutagenesis was performed to substitute Ser226/Ser255 with phosphomimetic
16 conditions (Glu226/Glu255) and de-phosphorylated conditions (Ala226/Ala255) in both protomers
17 of HSP90 β . The preparation of all complexes utilized the Protein Preparation Wizard, a module
18 for creating reliable, all-atom protein models. This involved restraining the assignment of bonds
19 and bond orders, adding hydrogens, correcting formal charges, and filling missing side chains.
20 Pre-processing steps included generating hetero states, H-bond assignment, and energy
21 minimization using the Optimized Potentials for Liquid Simulations (OPLS3) force field, with a
22 maximum root-mean-square deviation (RMSD) of 0.30 Å, employing the molecular mechanics
23 engine Impact v9.6. Essential water atoms within 5 Å of the binding pocket were retained, while
24 remaining waters were deleted. Structural refinement at neutral pH was carried out through the
25 Epik v6.1 module⁹². The final refined structure served as the receptor for docking simulations.
26 Ligands, such as ATP and ADP, underwent preparation with the LigPrep node, where the
27 optimized ligand minimization algorithm yielded more conformers with numerous rotatable bonds,
28 enhanced efficiency, and robustness. Different possible protonation states based on machine
29 learning were generated, and ligand structures were minimized at pH values within the range of
30 7.0 and +/- 2.0, to guide the selection of protonation states on acidic/basic groups on ligands
31 consistent with their pKa values, using the OPLS_3 force field, Premin, Truncated Newton
32 Conjugate Gradient (TNCG), and Epik v6.1 nodes. Subsequently, a receptor grid was generated
33 around the co-crystal ligand with default parameters. Docking experiments were executed on the
34 nucleotide binding pockets of both protomers using the XP (extra-precision) Glide program (Glide
35 v9.6) and Prime-MMGBSA (molecular mechanics generalized born surface area) modules,
36 respectively. The best poses in the resulting docked complexes served as the initial complex
37 structure for MD simulations⁹³. *Molecular dynamics simulations:* The pentameric assemblies were
38 prepared in the following combinations: 2xHSP90(Ser226Ser255)-2xHSP70-HOP,
39 2xHSP90(Glu226Glu255)-2xHSP70-HOP-, 2xHSP90(Ala226Ala255)-2xHSP70-HOP, each
40 bound to either ATP or ADP. These complexes underwent individual 100 ns all-atomic molecular
41 dynamics simulations using the Desmond v7.1 module of the MAESTRO Suite from Schrodinger
42 (www.schrodinger.com). Before simulations, each assembly was built by embedding water
43 molecules, adjusting temperature and pressure closer to the physiological environment through
44 the OPLS3 force field and TIP4PEW water model. The system was neutralized with counter ions
45 (Na⁺/ Cl⁻) to balance the net charge in the simulation box. The particle mesh Ewald (PME)
46 method⁹⁴ was used for electrostatics with a 10 Å cut-off for Lennard-Jones interactions, and the
47 SHAKE algorithm⁹⁵ was applied to restrict the motion of all covalent bonds involving hydrogen
48 atoms. The complex system underwent a six-step relaxation protocol before productive MD
49 simulations. The solvated system was initially minimized with solute restraints and then without
50 solute restraints, utilizing a hybrid method of steepest descent and the LBFGS (limited memory
51 Broyden-Fletcher-Goldfarb-Shanno) algorithm^{96,97}. The energy-minimized system underwent a

1 brief 12 ps simulation within the NVT canonical ensemble at a temperature of 10 K, followed by a
2 similar simulation in the isothermal-isobaric (NPT) ensemble at 10 K, with restraints on
3 nonhydrogen solute atoms. Subsequently, the system was simulated for 24 ps in the NPT
4 ensemble at 300 K with limited restraints on nonhydrogen solute atoms. In the final equilibration
5 step, the system was simulated for 24 ps in the NPT ensemble at 300 K without constraints to
6 reach an equilibrium state. The minimized and equilibrated system without restraints was then
7 subjected to a 100 ns NPT simulation for production. The temperatures and pressures of the
8 system in the initial simulations were controlled by Berendsen thermostats and barostats,
9 respectively^{96,97}. The relaxed system underwent productive simulations using the Nose¹–Hoover
10 thermostat at 300 K and the Martyna–Tobias–Klein barostat at 1.01325 bar pressure. Atomic-
11 coordinate data for each receptor-ligand complex and system energies were recorded every 1000
12 ps. Residue-pair correlations were calculated along the MD trajectory using the script
13 `trj_essential_dynamics.py` available in the Schrödinger suite. Additionally, the unexplored cryptic
14 motions, distribution of secondary structural elements, and the array of protein folding in intrinsic
15 disordered regions were thoroughly examined using the extracted meta-trajectory data from 1000
16 trajectories throughout the simulation period. The secondary structure elements (SSE) index was
17 computed to illustrate the percentage occurrence of alpha-helices (α) and beta-strands (β) during
18 the simulation period, delineated by residue.

19 **Immunoprecipitation of mCherry-HSP90**

20 RFP Selector (NanoTag #N0410) resins were equilibrated with lysis buffer to prepare the resin.
21 Cell lysates were then added and incubated with the resins at 4°C with head over tail rotation for
22 90 min. Following incubation, resins were washed twice with lysis buffer and once with PBS before
23 elution with 2 × sample buffer and incubation at 95°C for 5 min. Eluents were then run on a 12.5%
24 SDS-PAGE. For SILAC samples, heavy and light replicates were immunoprecipitated separately,
25 before combined and separated by SDS gel electrophoresis.

26 **Chemical cross-linking**

27 Cell lysates, with a concentration of approximately 3 $\mu\text{g } \mu\text{L}^{-1}$, underwent cross-linking using
28 disuccinimidyl suberate (DSS; ThermoFisher# 21655) at a concentration of 2.5 mM. This process
29 occurred at room temperature for 1 h. To terminate the reaction, 0.8 M NH_4OH (Sigma# 09859)
30 was added, reaching a final concentration of 25 mM, and incubated at room temperature for an
31 additional 15 min. The lysates were clarified through two rounds of centrifugation at 16,200× g for
32 15 min at 4°C before proceeding to separate HSP90 using immobilized PU-H71 or GA.

33 **SDS-PAGE and trypsin digestion**

34 After elution from PU- or GA-beads, samples were loaded into 12.5% SDS-PAGE gel for
35 separation. The entire lanes were cut into 10-15 bands and processed by in-gel digestion as
36 described previously¹⁹. Briefly, gel bands were cut into small cubes, washed with 25 mM
37 NH_4HCO_3 /50% acetonitrile, reduced with 10 mM DTT (in 25 mM NH_4HCO_3) at 56°C for 1 h,
38 alkylated with 55 mM iodoacetamide (in 25 mM NH_4HCO_3) in darkness for 45 min. Gel pieces
39 were washed again with 25 mM NH_4HCO_3 /50% acetonitrile and evaporated in a speed-vac to
40 complete dryness. The dried gel samples were proteolyzed using varied volumes of trypsin (0.6-
41 1.0 μg depending on the intensity of the gel bands) at 37°C for 4 h, before the extraction of tryptic
42 peptides by 50% acetonitrile/2% acetic acid. Tryptic peptide mixture was concentrated down to
43 ~7 μL before LC-MS/MS analysis. For validation experiments in **Figure 3d,e**, chemical
44 precipitation and sample preparation for PTM analyses were performed as follows. For in-cell YK-
45 B bait affinity purification, cells were plated in 10 cm plates at 6×10^6 cells per plate and treated
46 with 50 μM YK5-B for 4 h. Cells were next collected and lysed in 20 mM Tris pH 7.4, 150 mM
47 NaCl and 1% NP40 buffer. Five hundred micrograms (500 μg) of total protein were incubated with
48 streptavidin agarose beads (ThermoFisher Scientific) for 1 h and beads were washed with 20 mM
49

1 Tris pH 7.4, 100 mM NaCl and 0.1% NP40 buffer (washing buffer). For in-lysate YK5-B bait affinity
2 purification, cells were lysed in the above-mentioned lysis buffer. Streptavidin agarose beads
3 were incubated with 50 μ M YK5-biotin for 1 h, washed and added to 500 μ g of total protein and
4 incubated overnight. The beads were then washed with the washing buffer. For PU-H71 beads
5 pull-down, 250 μ g of the same protein lysates were incubated with 40 μ l PU-H71 beads for 3 h
6 and washed. The samples were applied onto SDS-PAGE. Resulting gels were washed 3 times in
7 distilled deionized H₂O for 15 min each and visualized by staining overnight with Simply Blue
8 Coomassie stain (Thermo Fisher Scientific). Stained protein gel regions were typically excised
9 into 6 gel sections per gel lane, and completely destained as described¹⁹. In-gel digestion was
10 performed overnight with MS-grade trypsin (Trypsin Gold, Mass spectrometry grade, Promega)
11 at 5 ng mL⁻¹ in 50 mM NH₄HCO₃ digestion buffer and incubation at 37°C. After acidification with
12 10% formic acid (final concentration of 0.5-1% formic acid), peptides were extracted with 5%
13 formic acid / 50% acetonitrile and resulting peptides were desalted using hand-packed, reversed
14 phase Empore C18 Extraction Disks (3M, Cat#3M2215), following an established method⁹⁸. Each
15 of the 6 sections per sample, per gel lane, were excised and separately digested in-gel, at the
16 same time, using the same batch and amount of trypsin. The peptides from each of these gel
17 sections were purified and analyzed by nano-LC-MS/MS separately.

18 **LC-MS data acquisition, protein and phosphopeptide identification**

19 Briefly, the digestion mixtures were injected into an Dionex Ultimate 3000 RSLCnano UHPLC
20 system (Dionex Corporation, Sunnyvale, CA), and separated by a 75 μ m \times 25 cm PepMap RSLC
21 column (100 \AA , 2 μ m) at a flow rate of \sim 450 nL min⁻¹. The eluant was connected directly to a
22 nanoelectrospray ionization source of an LTQ Orbitrap XL mass spectrometer (Thermo Scientific,
23 Waltham, MA). LC-MS data were acquired in a data-dependent acquisition mode, cycling
24 between a MS scan (m/z 315–2,000) acquired in the Orbitrap, followed by low-energy CID
25 analysis on three most intense multiply charged precursors acquired in the linear ion trap. The
26 centroided peak lists of the CID spectra were generated using PAVA searched against a database
27 that is consisted of the Swiss-Prot protein database using Batch-Tag, a program of the University
28 of California San Francisco Protein Prospector software, version 5.9.2. For identification of
29 proteins in pull-down experiments, a precursor mass tolerance of 15 ppm and a fragment mass
30 tolerance of 0.5 Da were used for protein database searches (trypsin as enzyme; 1 miscleavage;
31 carbamidomethyl (C) as constant modification; acetyl (protein N-term), acetyl+oxidation (protein
32 N-term), Met-loss (protein N-term), Met-loss+acetyl (protein N-term, oxidation (M)). Protein hits
33 were reported with a Protein Prospector protein score \geq 22, a protein discriminant score \geq 0.0 and
34 a peptide expectation value \leq 0.01⁹⁹. This set of thresholds of protein identification parameters
35 does not return any substantial false positive protein hits from the randomized half of the
36 concatenated database. After protein identification, PTM search was carried out with S/T/Y
37 phosphorylation included in variable modifications among the identified proteins. A threshold of
38 SLIP score $>$ 6 was imposed for false phosphorylation site assignment $<$ 5%¹⁰⁰. Identified
39 phosphopeptides were manually inspected by confirming the quality of MS/MS spectra and mass
40 accuracy. Cross-linked peptides were identified using an integrated module in Protein Prospector,
41 based on a bioinformation strategy developed in the UCSF Mass Spectrometry Facility^{41,42,101,102}.
42 Key cross-linked peptides were identified and confirmed by manually examining the returned
43 spectrum, peptide scores, mass accuracy and absence from uncross-linked samples. For
44 validation experiments in Figure 3e, MS data acquisition and processing were performed as
45 follows. Desalted peptides were concentrated to a very small droplet by vacuum centrifugation
46 and reconstituted in 10 mL 0.1% formic acid in H₂O. Approximately 90% of the peptides were
47 analyzed by nano-LC-MS/MS). A Q Exactive HF mass spectrometer was coupled directly to an
48 EASY-nLC 1000 (Thermo Fisher Scientific) equipped with a self-packed 75 mm \times 18 cm reverse
49 phase column (ReproSil-Pur C18, 3M, Dr. Maisch GmbH, Germany) for peptide separation.
50 Analytical column temperature was maintained at 50°C by a column oven (Sonation GmbH,

1 Germany). Peptides were eluted with a 3-40% acetonitrile gradient over 60 min at a flow rate of
2 250 nL min⁻¹. The mass spectrometer was operated in DDA mode with survey scans acquired at
3 a resolution of 120,000 (at m/z 200) over a scan range of 300-1750 m/z. Up to 15 of the most
4 abundant precursors from the survey scan were selected with an isolation window of 1.6 Th for
5 fragmentation by higher-energy collisional dissociation with normalized collision energy (NCE) of
6 27. The maximum injection time for the survey and MS/MS scans was 20 ms and 60 ms,
7 respectively; the ion target value (Automatic Gain Control) for survey and MS/MS scan modes
8 was set to 3e⁶ and 1e⁶, respectively.

9 **Quantitation of phosphopeptides and crosslinked peptides**

11 Manually-confirmed, high-confidence phosphopeptides and cross-linked peptides were quantified
12 by the peak height of the extracted ion chromatogram of each peptide monoisotope mass. For
13 phosphopeptide quantitation, the protein loading of HSP90 peptides in lysates or from pull-down
14 experiments was normalized to a representative, isoform specific tryptic peptide, ELISNSSDALDK
15 for HSP90 α and ELISNASDALDK for HSP90 β . Phosphopeptides with different charge state or
16 miscleavages were considered as different measurements for quantitation of each phosphosite.
17 To assess the relative phosphorylation levels of different phosphosites in cancer cells and non-
18 transformed cells, the ion intensity values of all phosphopeptides for each phosphosite were
19 summed. The average ion intensities of each phosphosite between cancer and non-transformed
20 cells were compared. Cross-linked peptides were identified using an integrated module in Protein
21 Prospector, based on a bioinformatics strategy developed in the UCSF Mass Spectrometry
22 Facility^{41,42,101,102}. Key cross-linked peptides were identified and confirmed by manually examining
23 the returned spectrum, peptide scores, mass accuracy and absence from uncross-linked
24 samples. Cross-linked peptides identified from various samples were pooled together, and the
25 cross-linking propensity of each cross-linked peptide was assessed by its cross-linking
26 percentage⁴³. Cross-linking percentage for each peptide pair was calculated using the following
27 formula:

$$28 \quad \%XL = \frac{\text{Cross - linked peptide Peak Height (PH)}}{\sum \text{Cross - linked peptide PH} + \text{Dead - end XL 1 PH} + \text{Dead - end XL 2 PH}}$$

29
30 where the peak height is the apex peak height in LC-MS/MS runs. Dead-end XLs are cross-
31 linker modified peptides where only one NHS-ester function of DSS is cross-linked to a Lys
32 residue and the other NHS-ester function is hydrolyzed by water.

33 **Homology modeling**

34 The mouse HSP90 sequences for both alpha and beta isoforms were aligned and the models
35 were built using an open conformation template (PDB: 2IQO), a closed conformation template
36 (PDB: 2CG9), and an HSP70-bound model (derived from a cryo-EM structure of
37 HSP90•HSP70•GR complex¹⁰ using UCSF Modeller. Structural visualization and analysis were
38 carried out using UCSF Chimera.

39 **Statistics and reproducibility**

40 Unless as specified above under Protein identification and Bioinformatics analyses, statistics were
41 performed, and graphs were generated, using Prism 10 software (GraphPad). Statistical
42 significance was determined using Student's t-Tests or ANOVA, as indicated. Means and
43 standard errors were reported for all results unless otherwise specified. Effects achieving 95%
44 confidence interval (i.e., $p < 0.05$) were interpreted as statistically significant. No statistical
45 methods were used to pre-determine sample sizes, but these are similar to those generally
46 employed in the field. No samples were excluded from any analysis unless explicitly stated.

1 **Reporting summary.** Further information on research design is available in the Nature Research
2 Reporting Summary linked to this article.

3 **DATA AVAILABILITY**

4 The source data underlying all main and supplementary figures are provided with this paper as a
5 Source Data file. Datasets and analytics associated with epichaperomics and proteomics
6 analyses are available in the Supplementary Information as Supplementary Data 1 through 6. LC-
7 MS data (i.e., proteomics and epichaperomics raw mass spectrometry data, peak lists, and
8 results) that support the findings of this study are deposited to the ProteomeXchange Consortium
9 via the PRIDE partner repository with the dataset identifier PXD050251 [**Reviewer account**
10 **details:** Username: reviewer_pxd050251@ebi.ac.uk; Password: TmZMDQ0W]. Protein
11 sequences (FASTA files) were obtained from UniProt (<https://www.uniprot.org/>). MD simulations
12 data were deposited in Zenodo [[https://doi.org/ 10.5281/zenodo.10800912](https://doi.org/10.5281/zenodo.10800912)]¹⁰³. Source data are
13 provided with this paper.
14

15 **CODE AVAILABILITY**

16 No code was developed during this study.

17 **REFERENCES**

- 18 1. Bludau, I. & Aebersold, R. Proteomic and interactomic insights into the molecular basis of
19 cell functional diversity. *Nat. Rev. Mol. Cell Biol.* **21**, 327-340 (2020).
- 20 2. Nussinov, R., Tsai, C. J. & Jang, H. Protein ensembles link genotype to phenotype. *PLoS*
21 *Comput. Biol.* **15**, e1006648 (2019).
- 22 3. Chiosis, G., Digwal, C. S., Trepel, J. B. & Neckers, L. Structural and functional complexity
23 of HSP90 in cellular homeostasis and disease. *Nat. Rev. Mol. Cell Biol.* **24**, 797-815
24 (2023).
- 25 4. Schopf, F. H., Biebl, M. M. & Buchner, J. The HSP90 chaperone machinery. *Nat. Rev.*
26 *Mol. Cell Biol.* **18**, 345-360 (2017).
- 27 5. Krukenberg, K. A., Street, T. O., Lavery, L. A. & Agard, D. A. Conformational dynamics of
28 the molecular chaperone Hsp90. *Q. Rev. Biophys.* **44**, 229-255 (2011).
- 29 6. Biebl, M. M. & Buchner, J. Structure, Function, and Regulation of the Hsp90 Machinery.
30 *Cold Spring Harb. Perspect. Biol.* **11**, (2019).
- 31 7. Street, T. O., Lavery, L. A., Verba, K. A., Lee, C. T., Mayer, M. P. & Agard, D. A. Cross-
32 monomer substrate contacts reposition the Hsp90 N-terminal domain and prime the
33 chaperone activity. *J. Mol. Biol.* **415**, 3-15 (2012).
- 34 8. Street, T. O., Lavery, L. A. & Agard, D. A. Substrate binding drives large-scale
35 conformational changes in the Hsp90 molecular chaperone. *Mol. Cell* **42**, 96-105 (2011).
- 36 9. Street, T. O. et al. Elucidating the mechanism of substrate recognition by the bacterial
37 Hsp90 molecular chaperone. *J. Mol. Biol.* **426**, 2393-2404 (2014).
- 38 10. Wang, R. Y., Noddings, C. M., Kirschke, E., Myasnikov, A. G., Johnson, J. L. & Agard, D.
39 A. Structure of Hsp90-Hsp70-Hop-GR reveals the Hsp90 client-loading mechanism.
40 *Nature* **601**, 460-464 (2022).
- 41 11. Dean, M. E. & Johnson, J. L. Human Hsp90 cochaperones: perspectives on tissue-specific
42 expression and identification of cochaperones with similar in vivo functions. *Cell Stress*
43 *Chaperones* **26**, 3-13 (2021).
- 44 12. Backe, S. J., Sager, R. A., Woodford, M. R., Makedon, A. M. & Mollapour, M. Post-
45 translational modifications of Hsp90 and translating the chaperone code. *J. Biol. Chem.*
46 **295**, 11099-11117 (2020).

- 1 13. Rodina, A. et al. The epichaperome is an integrated chaperome network that facilitates
2 tumour survival. *Nature* **538**, 397-401 (2016).
- 3 14. Svirsky, S. E., Li, Y., Henchir, J., Rodina, A., Carlson, S. W., Chiosis, G. & Dixon, C. E.
4 Experimental traumatic brain injury increases epichaperome formation. *Neurobiol. Dis.*
5 **188**, 106331 (2023).
- 6 15. Inda, M. C. et al. The epichaperome is a mediator of toxic hippocampal stress and leads
7 to protein connectivity-based dysfunction. *Nat. Commun.* **11**, 319 (2020).
- 8 16. Ginsberg, S. D., Joshi, S., Sharma, S., Guzman, G., Wang, T., Arancio, O. & Chiosis, G.
9 The penalty of stress - Epichaperomes negatively reshaping the brain in
10 neurodegenerative disorders. *J. Neurochem.* **159**, 958-979 (2021).
- 11 17. Joshi, S., Wang, T., Araujo, T. L. S., Sharma, S., Brodsky, J. L. & Chiosis, G. Adapting to
12 stress - chaperome networks in cancer. *Nat. Rev. Cancer* **18**, 562-575 (2018).
- 13 18. Ginsberg, S. D., Sharma, S., Norton, L. & Chiosis, G. Targeting stressor-induced
14 dysfunctions in protein-protein interaction networks via epichaperomes. *Trends*
15 *Pharmacol. Sci.* **44**, 20-33 (2023).
- 16 19. Rodina, A. et al. Systems-level analyses of protein-protein interaction network
17 dysfunctions via epichaperomics identify cancer-specific mechanisms of stress
18 adaptation. *Nat. Commun.* **14**, 3742 (2023).
- 19 20. Kishinevsky, S. et al. HSP90-incorporating chaperome networks as biosensor for disease-
20 related pathways in patient-specific midbrain dopamine neurons. *Nat. Commun.* **9**, 4345
21 (2018).
- 22 21. Zong, H. et al. A Hyperactive Signalosome in Acute Myeloid Leukemia Drives Addiction
23 to a Tumor-Specific Hsp90 Species. *Cell Rep.* **13**, 2159-2173 (2015).
- 24 22. Sugita, M. et al. Targeting the epichaperome as an effective precision medicine approach
25 in a novel PML-SYK fusion acute myeloid leukemia. *NPJ Precis. Oncol.* **5**, 44 (2021).
- 26 23. Bolaender, A. et al. Chemical tools for epichaperome-mediated interactome dysfunctions
27 of the central nervous system. *Nat. Commun.* **12**, 4669 (2021).
- 28 24. Araki, R. et al. Crucial role of c-Myc in the generation of induced pluripotent stem cells.
29 *Stem Cells* **29**, 1362-1370 (2011).
- 30 25. Varlakhanova, N. V. et al. myc maintains embryonic stem cell pluripotency and self-
31 renewal. *Differentiation* **80**, 9-19 (2010).
- 32 26. Wang, J. et al. c-Myc is required for maintenance of glioma cancer stem cells. *PLoS One*
33 **3**, e3769 (2008).
- 34 27. Kourtis, N. et al. Oncogenic hijacking of the stress response machinery in T cell acute
35 lymphoblastic leukemia. *Nat. Med.* **24**, 1157-1166 (2018).
- 36 28. Sharma, S. et al. Unraveling the Mechanism of Epichaperome Modulation by Zelavespib:
37 Biochemical Insights on Target Occupancy and Extended Residence Time at the Site of
38 Action. *Biomedicines* **11**, (2023).
- 39 29. Minami, Y., Kawasaki, H., Miyata, Y., Suzuki, K. & Yahara, I. Analysis of native forms and
40 isoform compositions of the mouse 90-kDa heat shock protein, HSP90. *J. Biol. Chem.*
41 **266**, 10099-10103 (1991).
- 42 30. Pillarsetty, N. et al. Paradigms for Precision Medicine in Epichaperome Cancer Therapy.
43 *Cancer Cell* **36**, 559-573.e557 (2019).
- 44 31. Niwa, H., Miyazaki, J. & Smith, A. G. Quantitative expression of Oct-3/4 defines
45 differentiation, dedifferentiation or self-renewal of ES cells. *Nat. Genet.* **24**, 372-376
46 (2000).
- 47 32. Lee, J., Go, Y., Kang, I., Han, Y. M. & Kim, J. Oct-4 controls cell-cycle progression of
48 embryonic stem cells. *Biochem. J.* **426**, 171-181 (2010).
- 49 33. Kurosawa, H. Methods for inducing embryoid body formation: in vitro differentiation
50 system of embryonic stem cells. *J Biosci Bioeng* **103**, 389-398 (2007).

- 1 34. Miller, J. D. et al. Human iPSC-based modeling of late-onset disease via progerin-induced
2 aging. *Cell Stem Cell* **13**, 691-705 (2013).
- 3 35. Moullick, K. et al. Affinity-based proteomics reveal cancer-specific networks coordinated
4 by Hsp90. *Nat. Chem. Biol.* **7**, 818-826 (2011).
- 5 36. Chen, P. B. et al. Hdac6 regulates Tip60-p400 function in stem cells. *Elife* **2**, e01557
6 (2013).
- 7 37. Brickner, D. G. et al. Transcription factor binding to a DNA zip code controls
8 interchromosomal clustering at the nuclear periphery. *Dev. Cell* **22**, 1234-1246 (2012).
- 9 38. Beebe, K. et al. Posttranslational modification and conformational state of heat shock
10 protein 90 differentially affect binding of chemically diverse small molecule inhibitors.
11 *Oncotarget* **4**, 1065-1074 (2013).
- 12 39. Maiti, S. & Picard, D. Cytosolic Hsp90 Isoform-Specific Functions and Clinical
13 Significance. *Biomolecules* **12**, (2022).
- 14 40. Chu, F. et al. Unraveling the interface of signal recognition particle and its receptor by
15 using chemical cross-linking and tandem mass spectrometry. *Proc. Natl. Acad. Sci. U. S.*
16 *A.* **101**, 16454-16459 (2004).
- 17 41. Karagoz, G. E., Acosta-Alvear, D., Nguyen, H. T., Lee, C. P., Chu, F. & Walter, P. An
18 unfolded protein-induced conformational switch activates mammalian IRE1. *Elife* **6**,
19 (2017).
- 20 42. Chu, F., Thornton, D. T. & Nguyen, H. T. Chemical cross-linking in the structural analysis
21 of protein assemblies. *Methods* **144**, 53-63 (2018).
- 22 43. Chu, F., Hogan, D., Gupta, R., Gao, X. Z., Nguyen, H. T. & Cote, R. H. Allosteric
23 Regulation of Rod Photoreceptor Phosphodiesterase 6 (PDE6) Elucidated by Chemical
24 Cross-Linking and Quantitative Mass Spectrometry. *J. Mol. Biol.* **431**, 3677-3689 (2019).
- 25 44. Stebbins, C. E., Russo, A. A., Schneider, C., Rosen, N., Hartl, F. U. & Pavletich, N. P.
26 Crystal structure of an Hsp90-geldanamycin complex: targeting of a protein chaperone by
27 an antitumor agent. *Cell* **89**, 239-250 (1997).
- 28 45. Huck, J. D., Que, N. L. S., Sharma, S., Taldone, T., Chiosis, G. & Gewirth, D. T. Structures
29 of Hsp90alpha and Hsp90beta bound to a purine-scaffold inhibitor reveal an exploitable
30 residue for drug selectivity. *Proteins* **87**, 869-877 (2019).
- 31 46. Immormino, R. M., Kang, Y., Chiosis, G. & Gewirth, D. T. Structural and quantum chemical
32 studies of 8-aryl-sulfanyl adenine class Hsp90 inhibitors. *J. Med. Chem.* **49**, 4953-4960
33 (2006).
- 34 47. Jeong, H., Kang, B. H. & Lee, C. Crystallization and preliminary X-ray diffraction analysis
35 of Trap1 complexed with Hsp90 inhibitors. *Acta Crystallogr F Struct Biol Commun* **70**,
36 1683-1687 (2014).
- 37 48. Prodromou, C., Roe, S. M., O'Brien, R., Ladbury, J. E., Piper, P. W. & Pearl, L. H.
38 Identification and structural characterization of the ATP/ADP-binding site in the Hsp90
39 molecular chaperone. *Cell* **90**, 65-75 (1997).
- 40 49. Ali, M. M. et al. Crystal structure of an Hsp90-nucleotide-p23/Sba1 closed chaperone
41 complex. *Nature* **440**, 1013-1017 (2006).
- 42 50. Castelli, M. et al. Molecular mechanisms of chaperone-directed protein folding: Insights
43 from atomistic simulations. *Protein Sci.* **33**, e4880 (2023).
- 44 51. Yan, P. et al. Molecular Stressors Engender Protein Connectivity Dysfunction through
45 Aberrant N-Glycosylation of a Chaperone. *Cell Rep.* **31**, 107840 (2020).
- 46 52. Wang, X. & Huang, L. Identifying dynamic interactors of protein complexes by quantitative
47 mass spectrometry. *Mol. Cell. Proteomics* **7**, 46-57 (2008).
- 48 53. Weidenauer, L. & Quadroni, M. Phosphorylation in the Charged Linker Modulates
49 Interactions and Secretion of Hsp90beta. *Cells* **10**, (2021).

- 1 54. Schlecht, R., Erbse, A. H., Bukau, B. & Mayer, M. P. Mechanics of Hsp70 chaperones
2 enables differential interaction with client proteins. *Nat. Struct. Mol. Biol.* **18**, 345-351
3 (2011).
- 4 55. Dhanasekaran, R., Deutzmann, A., Mahauad-Fernandez, W. D., Hansen, A. S., Gouw, A.
5 M. & Felsher, D. W. The MYC oncogene - the grand orchestrator of cancer growth and
6 immune evasion. *Nat. Rev. Clin. Oncol.* **19**, 23-36 (2022).
- 7 56. Chen, G., Yin, S., Zeng, H., Li, H. & Wan, X. Regulation of Embryonic Stem Cell Self-
8 Renewal. *Life (Basel)* **12**, (2022).
- 9 57. Mohiuddin, I. S., Wei, S. J. & Kang, M. H. Role of OCT4 in cancer stem-like cells and
10 chemotherapy resistance. *Biochim Biophys Acta Mol Basis Dis* **1866**, 165432 (2020).
- 11 58. Joshi, S. et al. Pharmacologically controlling protein-protein interactions through
12 epichaperomes for therapeutic vulnerability in cancer. *Commun. Biol.* **4**, 1333 (2021).
- 13 59. Carter, B. Z. et al. Epichaperome inhibition targets TP53-mutant AML and AML
14 stem/progenitor cells. *Blood* **142**, 1056-1070 (2023).
- 15 60. Yang, J. et al. Guidelines and definitions for research on epithelial-mesenchymal
16 transition. *Nat. Rev. Mol. Cell Biol.* **21**, 341-352 (2020).
- 17 61. Scroggins, B. T. et al. An acetylation site in the middle domain of Hsp90 regulates
18 chaperone function. *Mol. Cell* **25**, 151-159 (2007).
- 19 62. Soroka, J., Wandinger, S. K., Mausbacher, N., Schreiber, T., Richter, K., Daub, H. &
20 Buchner, J. Conformational switching of the molecular chaperone Hsp90 via regulated
21 phosphorylation. *Mol. Cell* **45**, 517-528 (2012).
- 22 63. Mollapour, M. et al. Swe1Wee1-dependent tyrosine phosphorylation of Hsp90 regulates
23 distinct facets of chaperone function. *Mol. Cell* **37**, 333-343 (2010).
- 24 64. Mollapour, M. et al. Asymmetric Hsp90 N domain SUMOylation recruits Aha1 and ATP-
25 competitive inhibitors. *Mol. Cell* **53**, 317-329 (2014).
- 26 65. Xu, W. et al. Hsp90 middle domain phosphorylation initiates a complex conformational
27 program to recruit the ATPase-stimulating cochaperone Aha1. *Nat. Commun.* **10**, 2574
28 (2019).
- 29 66. Retzlaff, M., Stahl, M., Eberl, H. C., Lagleder, S., Beck, J., Kessler, H. & Buchner, J. Hsp90
30 is regulated by a switch point in the C-terminal domain. *EMBO Rep* **10**, 1147-1153 (2009).
- 31 67. Rehn, A. et al. A methylated lysine is a switch point for conformational communication in
32 the chaperone Hsp90. *Nat. Commun.* **11**, 1219 (2020).
- 33 68. Kundrat, L. & Regan, L. Identification of residues on Hsp70 and Hsp90 ubiquitinated by
34 the cochaperone CHIP. *J. Mol. Biol.* **395**, 587-594 (2010).
- 35 69. Jahn, M. et al. The charged linker of the molecular chaperone Hsp90 modulates domain
36 contacts and biological function. *Proc. Natl. Acad. Sci. U. S. A.* **111**, 17881-17886 (2014).
- 37 70. Lees-Miller, S. P. & Anderson, C. W. Two human 90-kDa heat shock proteins are
38 phosphorylated in vivo at conserved serines that are phosphorylated in vitro by casein
39 kinase II. *J. Biol. Chem.* **264**, 2431-2437 (1989).
- 40 71. Kim, S. W. et al. Casein Kinase 2 (CK2)-mediated Phosphorylation of Hsp90 β as a Novel
41 Mechanism of Rifampin-induced MDR1 Expression. *J. Biol. Chem.* **290**, 17029-17040
42 (2015).
- 43 72. Zakharia, K., Miyabe, K., Wang, Y., Wu, D., Moser, C. D., Borad, M. J. & Roberts, L. R.
44 Preclinical In Vitro and In Vivo Evidence of an Antitumor Effect of CX-4945, a Casein
45 Kinase II Inhibitor, in Cholangiocarcinoma. *Transl. Oncol.* **12**, 143-153 (2019).
- 46 73. St-Denis, N. A. & Litchfield, D. W. Protein kinase CK2 in health and disease: From birth to
47 death: the role of protein kinase CK2 in the regulation of cell proliferation and survival.
48 *Cell. Mol. Life Sci.* **66**, 1817-1829 (2009).
- 49 74. Buchou, T. et al. Disruption of the regulatory beta subunit of protein kinase CK2 in mice
50 leads to a cell-autonomous defect and early embryonic lethality. *Mol Cell Biol* **23**, 908-915
51 (2003).

- 1 75. Ruzzene, M. & Pinna, L. A. Addiction to protein kinase CK2: a common denominator of
2 diverse cancer cells? *Biochim Biophys Acta* **1804**, 499-504 (2010).
- 3 76. Borgo, C. et al. Generation and quantitative proteomics analysis of CK2alpha/alpha'((-/-))
4 cells. *Sci. Rep.* **7**, 42409 (2017).
- 5 77. Hanahan, D. Hallmarks of Cancer: New Dimensions. *Cancer Discov.* **12**, 31-46 (2022).
- 6 78. Labusca, L. & Mashayekhi, K. Human adult pluripotency: Facts and questions. *World J.*
7 *Stem Cells* **11**, 1-12 (2019).
- 8 79. Lee, L. J., Papadopoli, D., Jewer, M., Del Rincon, S., Topisirovic, I., Lawrence, M. G. &
9 Postovit, L. M. Cancer Plasticity: The Role of mRNA Translation. *Trends Cancer* **7**, 134-
10 145 (2021).
- 11 80. Rodina, A. et al. Identification of an allosteric pocket on human hsp70 reveals a mode of
12 inhibition of this therapeutically important protein. *Chem. Biol.* **20**, 1469-1480 (2013).
- 13 81. Kang, Y. et al. Heat shock protein 70 inhibitors. 1. 2,5'-thiodipyrimidine and 5-
14 (phenylthio)pyrimidine acrylamides as irreversible binders to an allosteric site on heat
15 shock protein 70. *J. Med. Chem.* **57**, 1188-1207 (2014).
- 16 82. Rodina, A. et al. Affinity purification probes of potential use to investigate the endogenous
17 Hsp70 interactome in cancer. *ACS Chem. Biol.* **9**, 1698-1705 (2014).
- 18 83. Taldone, T. et al. Heat shock protein 70 inhibitors. 2. 2,5'-thiodipyrimidines, 5-
19 (phenylthio)pyrimidines, 2-(pyridin-3-ylthio)pyrimidines, and 3-(phenylthio)pyridines as
20 reversible binders to an allosteric site on heat shock protein 70. *J. Med. Chem.* **57**, 1208-
21 1224 (2014).
- 22 84. Shrestha, L., Patel, H. J. & Chiosis, G. Chemical Tools to Investigate Mechanisms
23 Associated with HSP90 and HSP70 in Disease. *Cell Chem. Biol.* **23**, 158-172 (2016).
- 24 85. Taldone, T. et al. Design, synthesis, and evaluation of small molecule Hsp90 probes.
25 *Bioorg. Med. Chem.* **19**, 2603-2614 (2011).
- 26 86. Guasparri, I., Bubman, D. & Cesarman, E. EBV LMP2A affects LMP1-mediated NF-
27 kappaB signaling and survival of lymphoma cells by regulating TRAF2 expression. *Blood*
28 **111**, 3813-3820 (2008).
- 29 87. Hooper, M., Hardy, K., Handyside, A., Hunter, S. & Monk, M. HPRT-deficient (Lesch-
30 Nyhan) mouse embryos derived from germline colonization by cultured cells. *Nature* **326**,
31 292-295 (1987).
- 32 88. Roychowdhury, T., Santhaseela, A. R., Sharma, S., Panchal, P., Rodina, A. & Chiosis, G.
33 Use of Native-PAGE for the Identification of Epichaperomes in Cell Lines. *Methods Mol.*
34 *Biol.* **2693**, 175-191 (2023).
- 35 89. Corben, A. D. et al. Ex vivo treatment response of primary tumors and/or associated
36 metastases for preclinical and clinical development of therapeutics. *J. Vis. Exp.*, e52157
37 (2014).
- 38 90. Sali, A. & Blundell, T. L. Comparative protein modelling by satisfaction of spatial restraints.
39 *J. Mol. Biol.* **234**, 779-815 (1993).
- 40 91. Srivastava, D., Yadav, R. P., Singh, S., Boyd, K. & Artemyev, N. O. Unique interface and
41 dynamics of the complex of HSP90 with a specialized cochaperone AIPL1. *Structure* **31**,
42 309-317 e305 (2023).
- 43 92. Johnston, R. C. et al. Epik: pK(a) and Protonation State Prediction through Machine
44 Learning. *J. Chem. Theory Comput.* **19**, 2380-2388 (2023).
- 45 93. Castelli, M. et al. How aberrant N-glycosylation can alter protein functionality and ligand
46 binding: An atomistic view. *Structure* **31**, 987-1004.e1008 (2023).
- 47 94. Darden, T., York, D. & Pedersen, L. Particle Mesh Ewald - an N.Log(N) Method for Ewald
48 Sums in Large Systems. *J. Chem. Phys.* **98**, 10089-10092 (1993).
- 49 95. Ryckaert, J., Ciccotti, G. & Berendsen, H. J. C. Numerical integration of the cartesian
50 equations of motion of a system with constraints: molecular dynamics of n-alkanes. *J.*
51 *Comput. Phys.* **23**, 327-341 (1977).

- 1 96. Hayes, J. M. et al. Kinetics, in silico docking, molecular dynamics, and MM-GBSA binding
2 studies on prototype indirubins, KT5720, and staurosporine as phosphorylase kinase
3 ATP-binding site inhibitors: the role of water molecules examined. *Proteins* **79**, 703-719
4 (2011).
- 5 97. Shan, Y., Kim, E. T., Eastwood, M. P., Dror, R. O., Seeliger, M. A. & Shaw, D. E. How
6 does a drug molecule find its target binding site? *J. Am. Chem. Soc.* **133**, 9181-9183
7 (2011).
- 8 98. Rappsilber, J., Mann, M. & Ishihama, Y. Protocol for micro-purification, enrichment, pre-
9 fractionation and storage of peptides for proteomics using StageTips. *Nat. Protoc.* **2**, 1896-
10 1906 (2007).
- 11 99. Wu, T., Nance, J., Chu, F. & Fazio, T. G. Characterization of R-Loop-Interacting Proteins
12 in Embryonic Stem Cells Reveals Roles in rRNA Processing and Gene Expression. *Mol.*
13 *Cell. Proteomics* **20**, 100142 (2021).
- 14 100. Zhou, Y., Qiu, L., Sterpka, A., Wang, H., Chu, F. & Chen, X. Comparative
15 Phosphoproteomic Profiling of Type III Adenylyl Cyclase Knockout and Control, Male, and
16 Female Mice. *Front. Cell. Neurosci.* **13**, 34 (2019).
- 17 101. Chu, F., Baker, P. R., Burlingame, A. L. & Chalkley, R. J. Finding chimeras: a
18 bioinformatics strategy for identification of cross-linked peptides. *Mol. Cell. Proteomics* **9**,
19 25-31 (2010).
- 20 102. Zeng-Elmore, X. et al. Molecular architecture of photoreceptor phosphodiesterase
21 elucidated by chemical cross-linking and integrative modeling. *J. Mol. Biol.* **426**, 3713-
22 3728 (2014).
- 23 103. Pasala, C., Digwal, C. S., Sharma, S. & Chiosis, G. Molecular dynamics simulation data
24 associated with manuscript: Phosphorylation-Driven Epichaperome Assembly: A Critical
25 Regulator of Cellular Adaptability and Proliferation [Data set]. *Zenodo*,
26 <https://doi.org/10.5281/zenodo.10800912> (2024).
- 27 104. Kirschke, E., Goswami, D., Southworth, D., Griffin, P. R. & Agard, D. A. Glucocorticoid
28 receptor function regulated by coordinated action of the Hsp90 and Hsp70 chaperone
29 cycles. *Cell* **157**, 1685-1697 (2014).

30 **ACKNOWLEDGEMENTS**

31 This work was supported by the NIH (R01 CA172546, P01 CA186866, R56 AG061869, R01
32 HD09783, R01 AG067598, R01 AG074004, R01 AG072599, R56 AG072599, RF1 AG071805,
33 P30 CA08748, P20 GM113131), NSF GRFP (LB), UNH Hamel Center (HTN), UNH Graduate
34 School. G.Colombo acknowledges funding from Fondazione AIRC (Associazione Italiana
35 Ricerca Sul Cancro) under IG 2022 - ID. 27139. We thank Dr. David A. Agard for providing the
36 model of HSP90•HSP70•GR complex derived from a cryo-EM density map¹⁰⁴, Thomas G.
37 Fazio (U Mass Med School) for the E14 cells, Dr. Lorenz Studer for the human iPSCs and
38 iPSC-derived neurons, and Dana Levasseur (U Iowa) for the ZHBTc4 cells. We thank the
39 Molecular Cytology Core, the Antitumor Assessment Core and our colleagues in the
40 Departments of Surgery and Medicine at Memorial Sloan Kettering for providing the
41 biospecimens for research.

42 **AUTHOR CONTRIBUTIONS**

43 S.W.M performed the MS studies and biochemical and functional studies in mouse ESCs. T.R.
44 performed the biochemical and functional validation studies in human cells. C.P. performed the
45 MD simulations. H.T.N and D.T.T. performed MS studies of cargos and cross-linking experiments.
46 S.S. performed chemical synthesis, compound identity and purity evaluations for the
47 epichaperome probes. L.B. and N.Y. generated ESC culture samples and MS sample

1 preparation. A.R., P.P., S.J., S.C., S.B. and H.E-B. performed experiments. C.S.D. provided
2 reagents. V.M., C.K., J.L., P.Y., E.deS., A.C., S.M., and M.A. were involved in various aspects of
3 biospecimen handling, including recruitment, procurement, or processing at different stages from
4 surgery to delivery to the laboratory. R.J.C. and P.R.B. provided Protein Prospector and
5 supported data analysis. F.C., T.A.N., G.Chiosis and A.L.B. participated in the design and
6 analysis of various experiments. H.E-B., A.R., S.D.G., G.Colombo and T.A.N. assisted with
7 manuscript writing and data analysis. F.C. and G.C. developed the concept and wrote the paper.

8 **COMPETING INTERESTS**

9 Memorial Sloan Kettering Cancer Center holds the intellectual rights to the epichaperome
10 portfolio. G.C., A.R. and S.S. are inventors on the licensed intellectual property. All other authors
11 declare no competing interests.

12

13 **SUPPLEMENTARY INFORMATION**

14 **Supplementary Figures 1 through 9**

15 **Supplementary Note 1.** Synthesis and characterization of the chemical probes

16 **Supplementary Note 2.** Full nucleotide sequence of the HSP90 plasmids in FASTA format

17

18 **Supplementary Data 1** contains LC-MS data and data analysis of PU-H71 and GA pull-down
19 samples as well as 300 kDa band sliced from native-PAGE, associated with Figure 1d,1e, and
20 Supplementary Figure 2c,3.

21 **Supplementary Data 2** contains LC-MS data and data analysis for the identification and
22 quantitation of HSP90 cross-linked peptides in PU-H71 or GA pull-down samples, associated
23 with Figure 2b.

24 **Supplementary Data 3** contains LC-MS data analysis of the HSP90 band from PU-H71 pull-
25 down or lysate samples, associated with Figure 3b,3c.

26 **Supplementary Data 4** contains LC-MS data for SILAC quantitation of mCherry-HSP90 EE or
27 AA mutant pull-down experiments in three replicates, associated with Figure 6b,6c, and 8c.
28 Normalized median intensity SILAC ratios were used for quantitation.

29 **Supplementary Data 5** contains LC-MS data analysis for SILAC quantitation of
30 phosphopeptides from WT mcherry-HSP90 in ES or differentiated trophoblast state, associated
31 with Figure 8b.

32 **Supplementary Data 6** contains LC-MS data analysis for label-free quantitation of
33 phosphopeptides from the HSP90 band of PU-H71 or YK55 pull-down samples from a variety of
34 cell lines, associated with Figure 3d,3e.

35

Figure 1

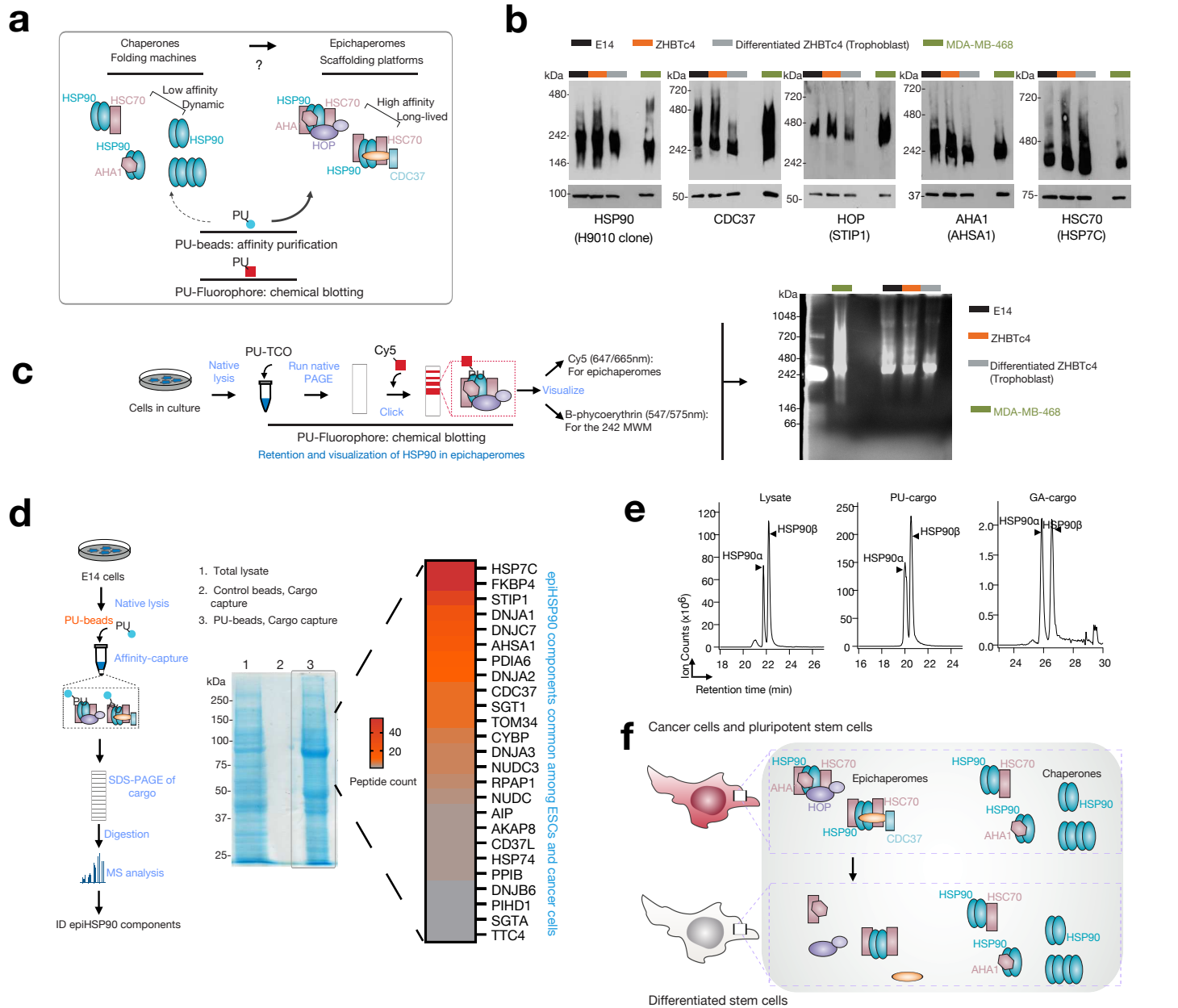


Figure 1. Embryonic stem cells and cancer cells share compositionally similar epichaperomes. **a** Schematic illustrating the biochemical and functional distinctions between epichaperomes, defined as long-lasting heterooligomeric assemblies composed of tightly associated chaperones and co-chaperones, and traditional chaperones. Unlike chaperones, which assist in protein folding or assembly, epichaperomes sequester proteins, reshaping protein-protein interactions, and consequently altering cellular phenotypes. The schematic also outlines key principles for the use of PU-probes in epichaperome analysis. **b** Detection of epichaperome components (chaperones and co-chaperones) through SDS-PAGE (bottom, total protein levels) and native-PAGE (top), followed by immunoblotting. See also Supplementary Fig. 1. **c** Visualization of HSP90 in epichaperomes using the PU-TCO click probe. See also Supplementary Fig. 2. Gel images are representative of three independent experiments. **d** Epichaperome constituent chaperones and co-chaperones identified through mass spectrometry analyses of PU-beads cargo. Representative data of two independent experiments. See Supplementary Fig. 3 for the GA-cargo. **e** Illustration of an isobaric, discriminant peptide pair from ESC lysate samples and HSP90 captured by PU- and GA-beads. Representative data of two independent experiments. **f** Schematic summary. Both cancer cells and pluripotent stem cells harbor epichaperomes. These epichaperomes undergo disassembly during differentiation processes. Source data are provided in Supplementary Data 1 and in Source data file.

Figure 2

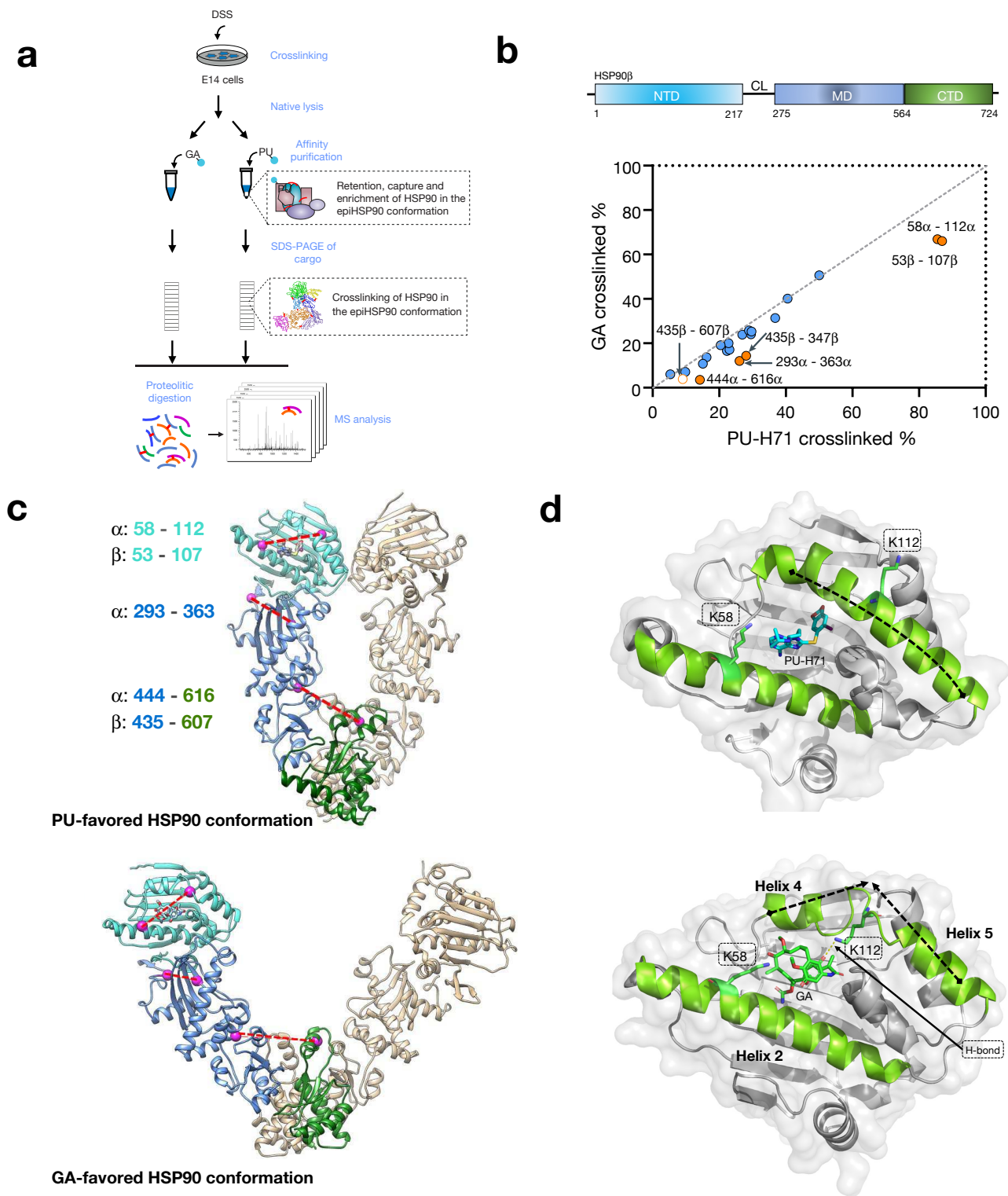


Figure 2. An enrichment of the closed-like conformation of HSP90 favors epichaperomes formation. **a** Experiment outline. **b** Plot comparing cross-linking propensity of Lys residues in HSP90 bound to PU-H71 or GA. Average cross-linking percentage of PU-H71 (x-axis) and GA (y-axis) bound HSP90 cross-linked pairs are shown. Blue circles represent pairs with similar cross-linking propensity (dotted line with a slope of 1). Orange points indicate outlier cross-linked peptides, with cross-linked Lys residues 8 amino acids away and the cross-linking percentage difference ≥ 1.5 standard deviation of replicates. Solid orange circles represent $p \leq 0.05$, $n = 3$ replicate measurements. **c** Homology model illustrating the HSP90 dimer in the open conformation (template PDB: 2IOQ), favored by geldanamycin (GA), and the closed conformation (template PDB: 2CG9), favored by PU-H71. One HSP90 protomer is colored to indicate the N-terminal domain (NTD, light blue), the middle domain (MD, dark blue), and the C-terminal domain (CTD, green). Cross-linked residues are labeled by pink dots and connected by red dashed lines. **d** NTD structures of PU-H71 (top, PDB: 2FWZ) and GA (bottom, PDB: 1YET)-bound HSP90. Source data are provided as Supplementary Data 2.

Figure 3

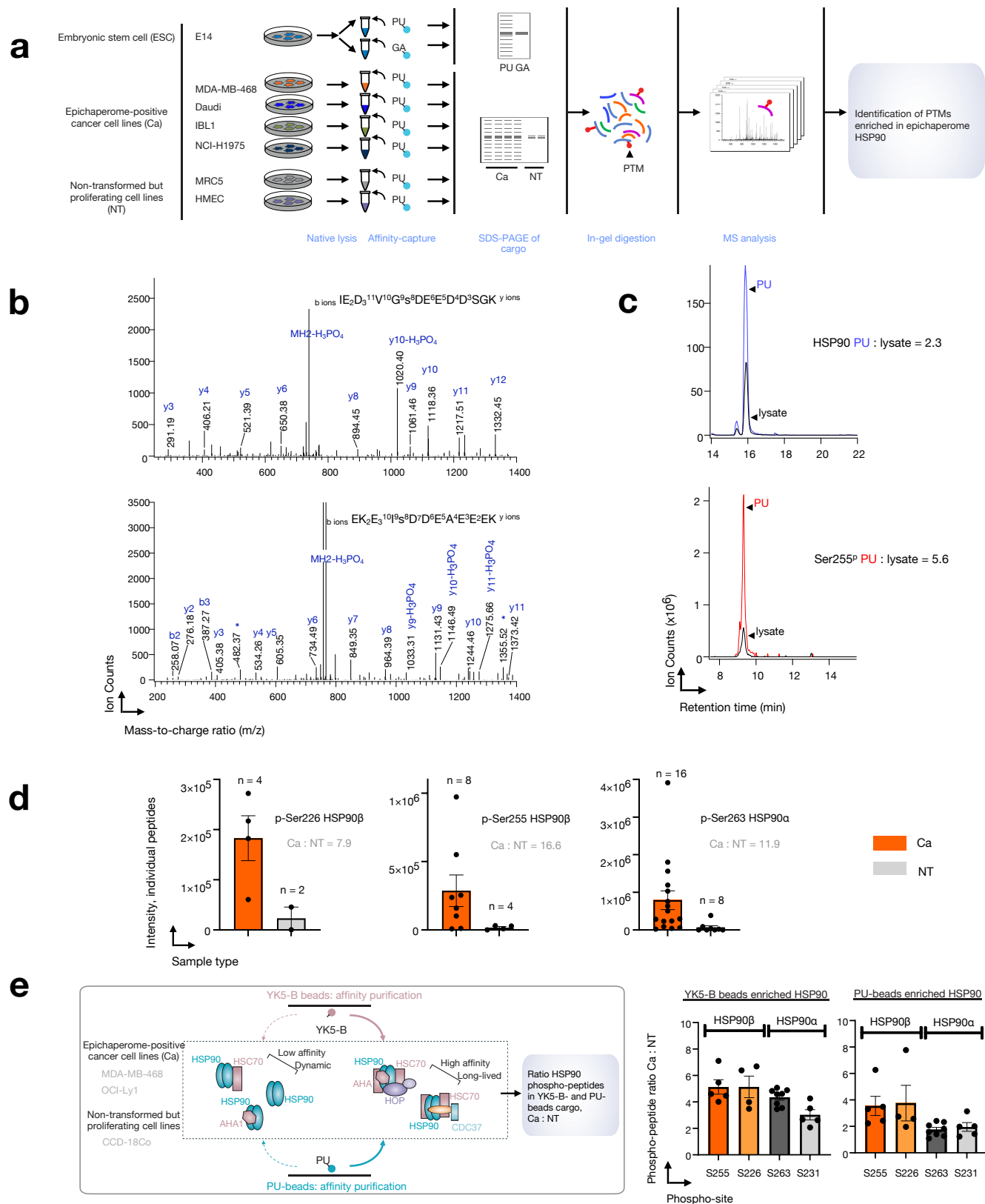


Figure 3. Phosphorylation of key residues located in the charged linker supports HSP90 incorporation into epichaperomes. **a** Experiment outline and expected outcomes. **b** Tandem MS spectra of HSP90 Ser226 (bottom) and Ser255 (top) phosphorylated peptides are presented, supporting the sequence and phosphorylation site identification. **c** Comparison of the extracted ion chromatogram of HSP90 Ser255 phosphopeptide in the PU-bead cargo (red trace, left panel) and ESC lysate (black trace, left panel) with a representative unmodified tryptic peptide in the PU-bead cargo (blue trace, right panel) and ESC lysate (black trace, right panel). **d** Ion intensity values of all phosphopeptides and the ratio of mean peptide intensity for each phosphosite in the samples described in panel a ($n = 4$ Ca and $n = 2$, NT). **e** Ratio of individual peptide intensity for each phosphosite in the samples described in the schematic (S255 $n = 5$; S226 $n = 4$; S263 $n = 8$; S231 $n = 5$). Source data are provided as Source Data file and as Supplementary Data 3,6.

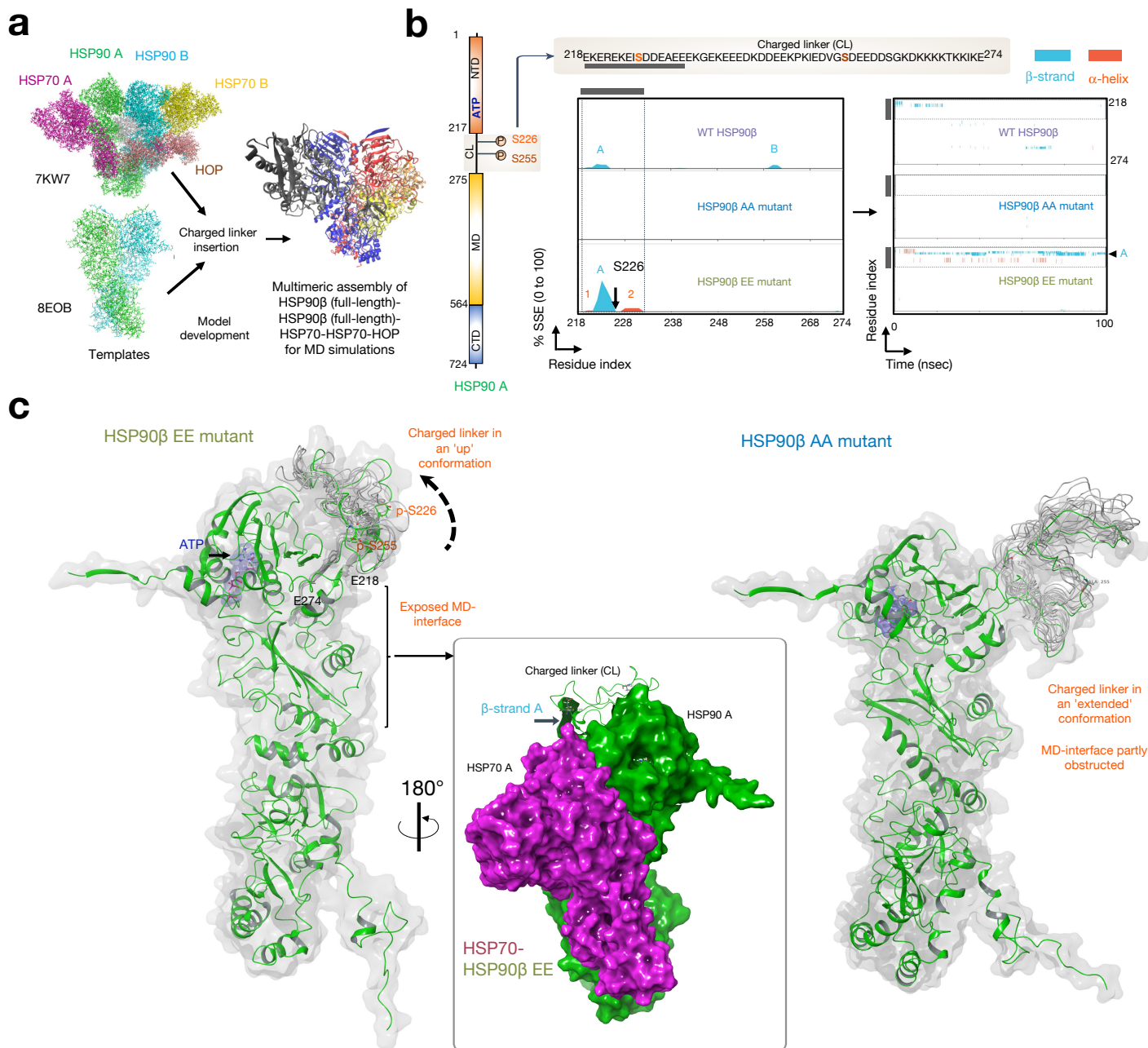
Figure 4

Figure 4. Phosphorylation of key residues located in the charged linker of HSP90 leads to a conformational shift in the linker, exposing the middle domain of the protein. **a** Model of the HSP90-HSP90-HSP70-HSP70-HOP assembly used for the molecular dynamics simulations. A and B, protomers A and B, respectively. **b** Protein secondary structure elements (SSE) like alpha-helices and beta-strands of the charged linker of protomer A of ATP-bound HSP90 monitored throughout the MD simulation. WT (HSP90 S226/S255), phosphomimetic (HSP90 S226E/S255E) and non-phosphorylatable (HSP90 S226A/S255A) mutants were analyzed. The plot on the left reports SSE distribution by residue index throughout the charged linker and the plot on the right monitors each residue and its SSE assignment over time. Schematic illustrating the primary structure of the full-length HSP90 with color-coded domains is also shown: NTD, N-terminal domain; MD, middle domain and CTD, C-terminal domain. The charged linker (CL) and the location of the two key serine residues are also shown (top inset). The gray bar indicates the CL segment encompassing residues 218 to 232. **c** Cartoon representation of ATP-bound HSP90 protomer A in assemblies containing the phosphomimetic (HSP90 S226E/S255E) or the non-phosphorylatable (HSP90 S226A/S255A) mutants is shown. Green, reference trajectory; gray, representative trajectories of $n = 1,000$. The inset illustrates the surfaces available for the interaction between HSP90 A and HSP70 A when the CL is in the 'up' conformation. A blue arrow indicates the location of the key beta-strand in the charged linker. See also Supplementary Figs. 5 and 6.

Figure 5

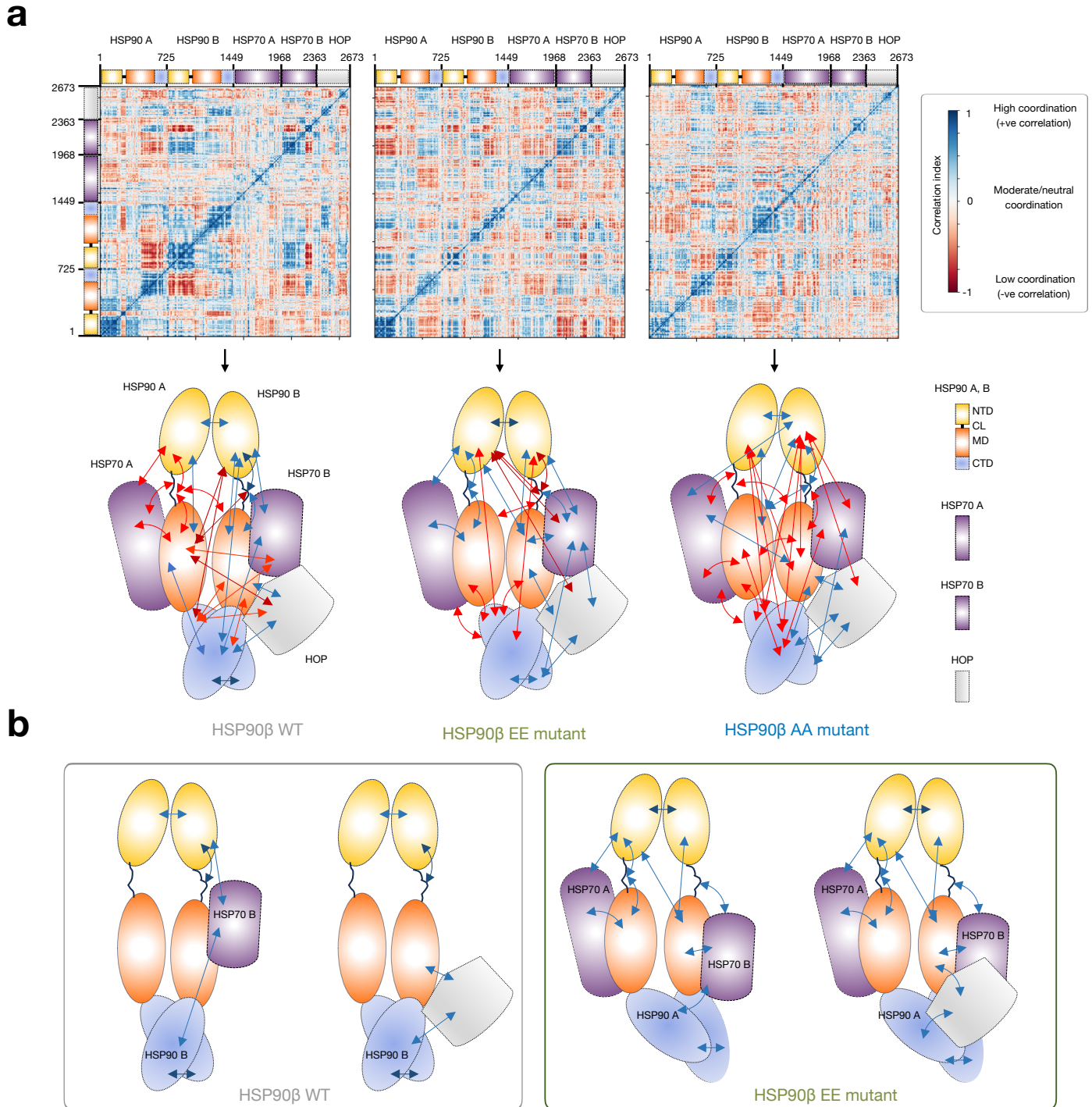


Figure 5. Phosphorylation of key residues located in the charged linker of HSP90 facilitates assembly motions conducive to epichaperome core formation. **a** Calculated dynamic cross-correlation matrix of Ca atoms around their mean positions for 100 ns molecular dynamics simulations. ATP-bound WT (HSP90 S226/S255), phosphomimetic (HSP90 S226E/S255E) and non-phosphorylatable (HSP90 S226A/S255A) mutant-containing HSP90-HSP90-HSP70-HSP70-HOP assemblies were analyzed. The cartoon below captures the key motions among the different domains of the individual assembly components. Extents of correlated motions and anti-correlated motions are color-coded from blue to red, which represent positive and negative correlations, respectively. The assembly contains two full-length HSP90beta proteins (protomer A and protomer B). The two HSP70 proteins (HSP70 A and HSP70 B) and the HOP protein are of sizes reported, and as per the constructs used in 7KW7. **b** Cartoon showing assemblies that are preferentially formed when the HSP90 charged linker is either phosphorylated (as in the EE mutant) or not phosphorylated (as in the WT protein).

Figure 6

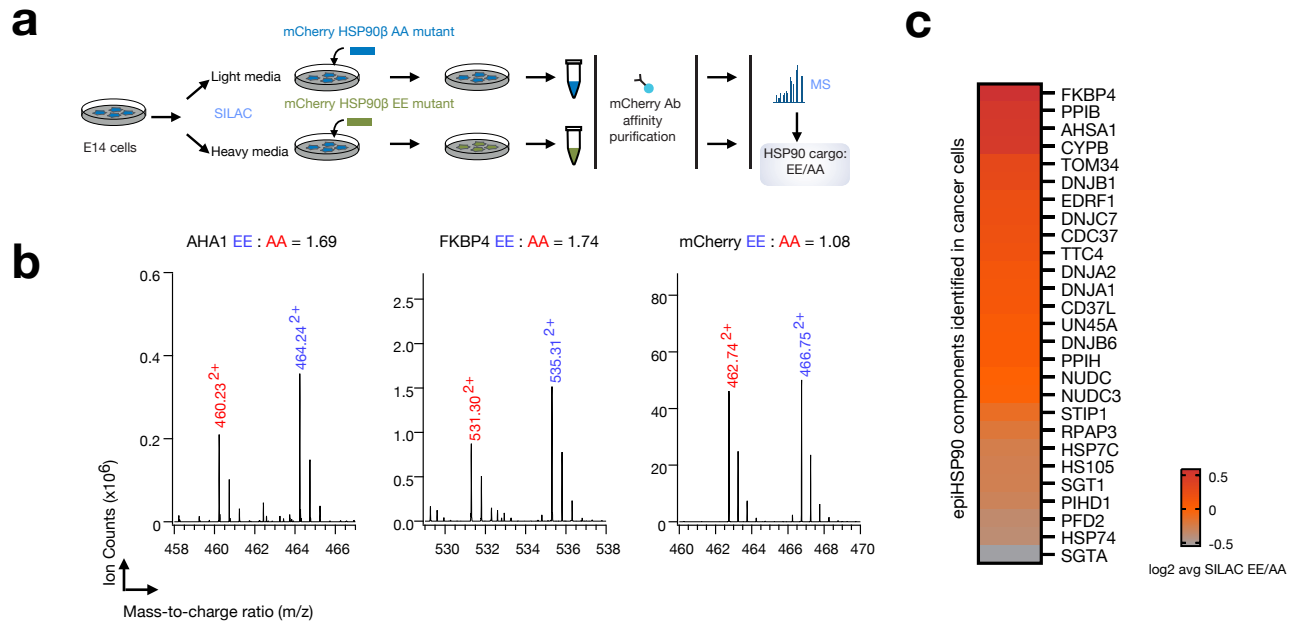


Figure 6. Immunopurification reveals increased presence of epichaperome-specific co-chaperones in phosphomimetic HSP90 complexes compared to non-phosphorylatable complexes. **a** Experiment outline and outcomes. **b** Representative spectra ($n = 3$ independent experiment) of proteins co-purified with the phosphomimetic HSP90^{S226E,S255E} (EE, blue) and non-phosphorylatable HSP90^{S226A,S255A} (AA, red) mutants. **c** Heatmap showing the identity of chaperone and co-chaperones identified as epichaperome components in cancer cells (as per Rodina et al. Nature 2016) and enriched in the affinity purified HSP90^{S226E,S255E} mutant. Scale bar, log₂ average SILAC values EE/AA ($n = 3$). Source data are provided as a Source Data file and as Supplementary Data 4.

Figure 7

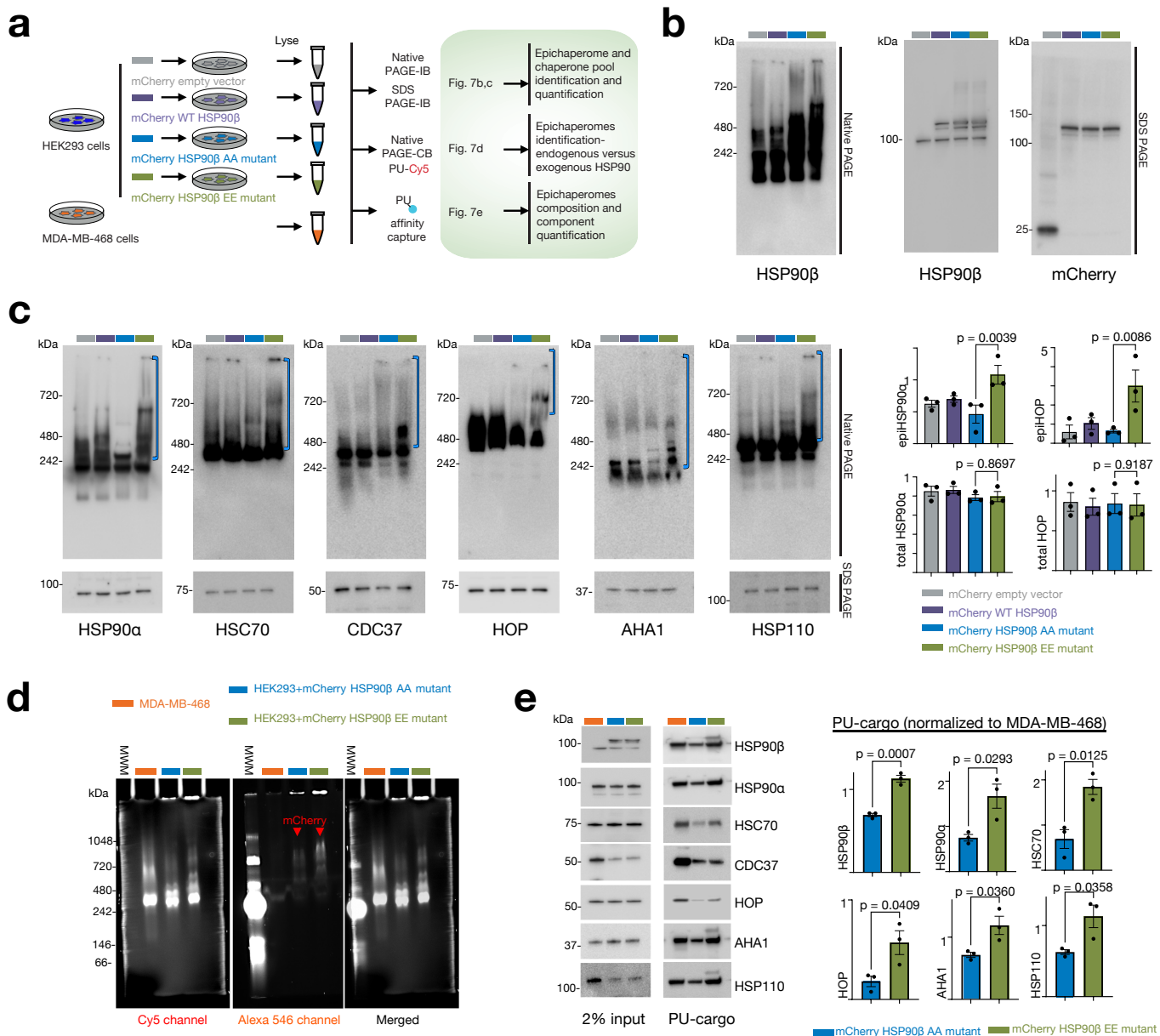


Figure 8

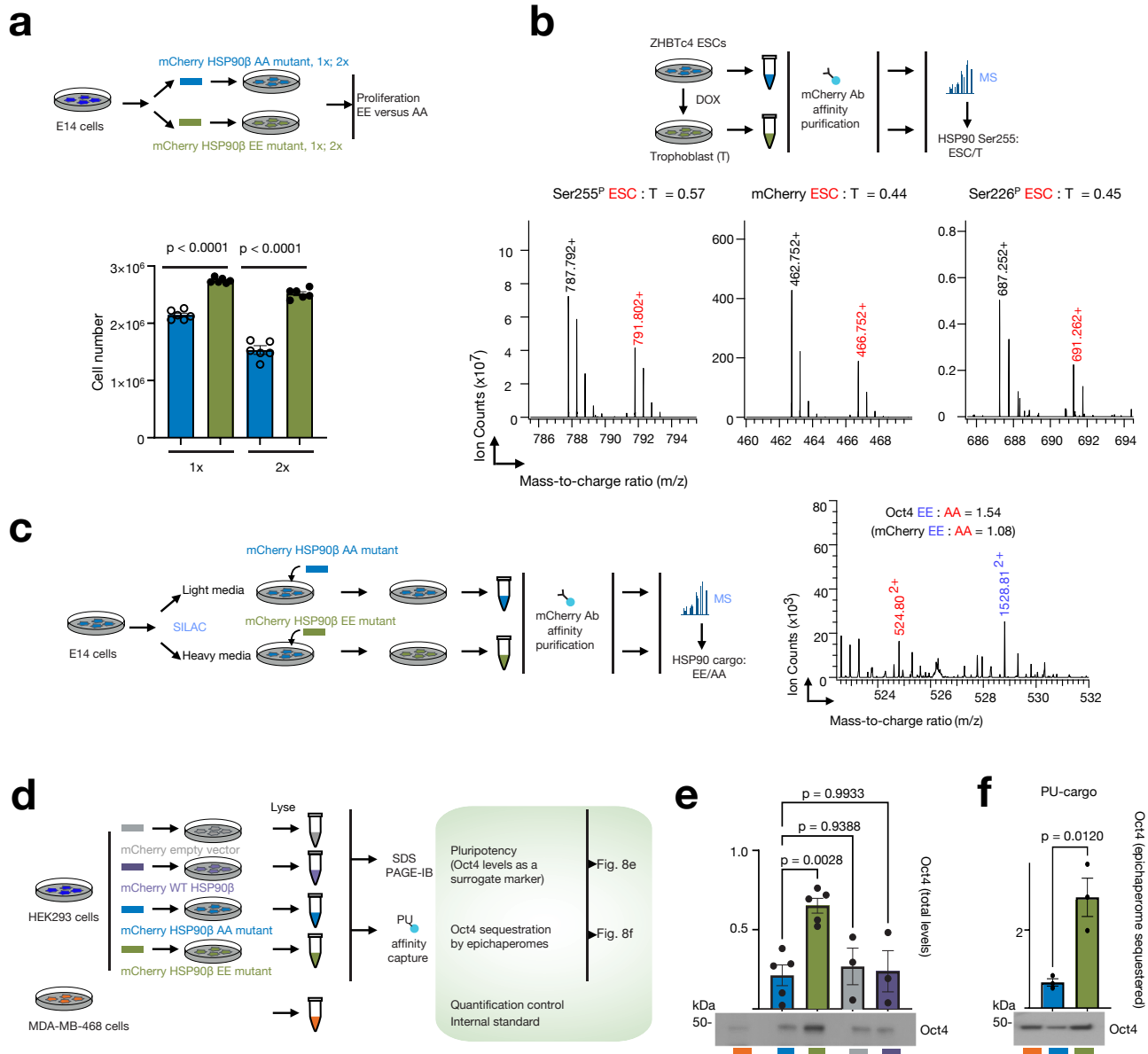


Figure 8. Phosphorylation of key residues located in the HSP90 charged linker favors ESC proliferation and self-renewal potential. **a** ESC proliferation at 60 h post-transfection in E14 cells transfected with either the phosphomimetic HSP90 β S226E,S255E (EE) or the nonphosphorylatable HSP90S226A,S255A (AA) mutant. Medium (1x) or high (2x) plasmid concentrations were employed. Data are presented as mean \pm s.e.m., $n = 6$, one-way ANOVA with Sidak's post-hoc, EE vs AA. **b** Representative spectra ($n = 3$ independent experiments) of phosphopeptides, S255P (left) and S226P (right), and a representative unmodified tryptic peptide (middle) in mCherry-tagged WT HSP90 β affinity-purified from ESC (red) or differentiated trophoblast (black) cells. **c** Representative spectra ($n = 3$ independent experiments) of a tryptic peptide from Oct4 protein co-purified from ESCs labeled with heavy or light isotope lysine and arginine expressing either the phosphomimetic (EE) or the non-phosphorylatable (AA) HSP90 mutant. Quantitative analysis via mass spectrometry (MS) to determine protein abundance is shown. **d** Overview of the experimental design and expected outcomes (panels e,f). **e,f** Detection and quantification of Oct4 protein expressed in cells transfected with the indicated HSP90 mutants or vector control (panel e) and sequestered into the epichaperome platforms (identified through PU-beads capture, panel f). (e) Data are presented as mean \pm s.e.m., $n = 5$ AA, $n = 5$ EE, $n = 3$ WT, $n = 3$ empty vector, one-way ANOVA with Dunnett's post-hoc, EE vs AA, WT vs AA, empty vector vs AA. (f) Data are presented as mean \pm s.e.m., $n = 3$, unpaired two-tailed t-test. Source data are provided as Source Data file and Supplementary Data 5.

Figure 9

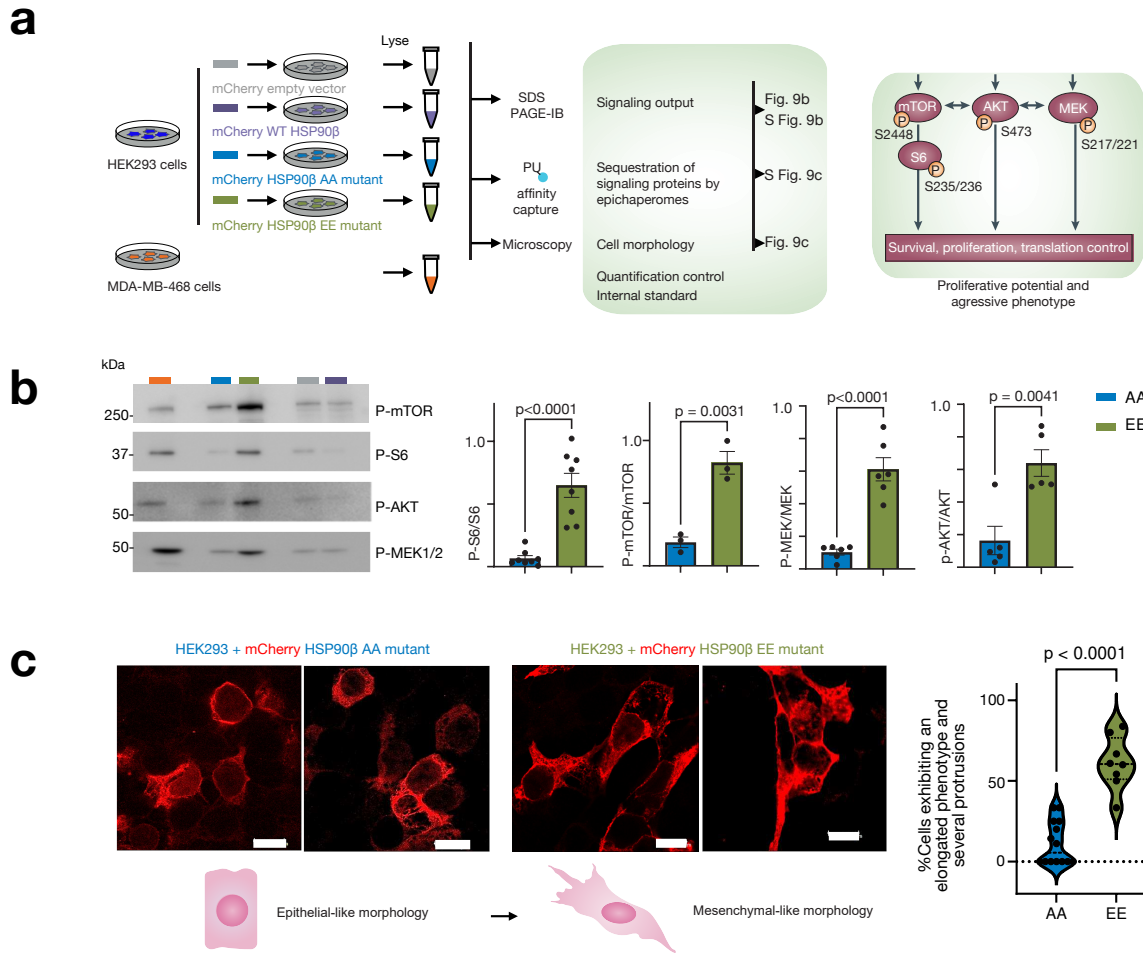


Figure 9. Regulation of epichaperome processes in ESC and cancer cells hinges on the specific phosphorylation events occurring at key residues within HSP90's charged linker. a Overview of the experimental design and expected outcomes. **b** Detection and quantification of proteins involved in transducing signaling events that lead to cell proliferation, survival, and protein synthesis control. See Supplementary Fig. 9 for total protein levels and levels sequestered into epichaperomes. Data are presented as mean \pm s.e.m., p-S6 n = 8; p-mTOR n = 3; p-MEK1/2 n = 6; p-AKT n = 5, unpaired two-tailed t-test. **c** Confocal microscopy shows morphological differences between the cells transfected with either the AA or the EE HSP90 mutant. Micrographs are representative of 96 cells for EE and 62 cells for AA. Scale bar, 10 μ m. Data are presented as mean \pm s.e.m., n = 8 wells for EE, n = 14 wells for AA, unpaired two-tailed t-test. Source data are provided as Source data file.

Figure 10

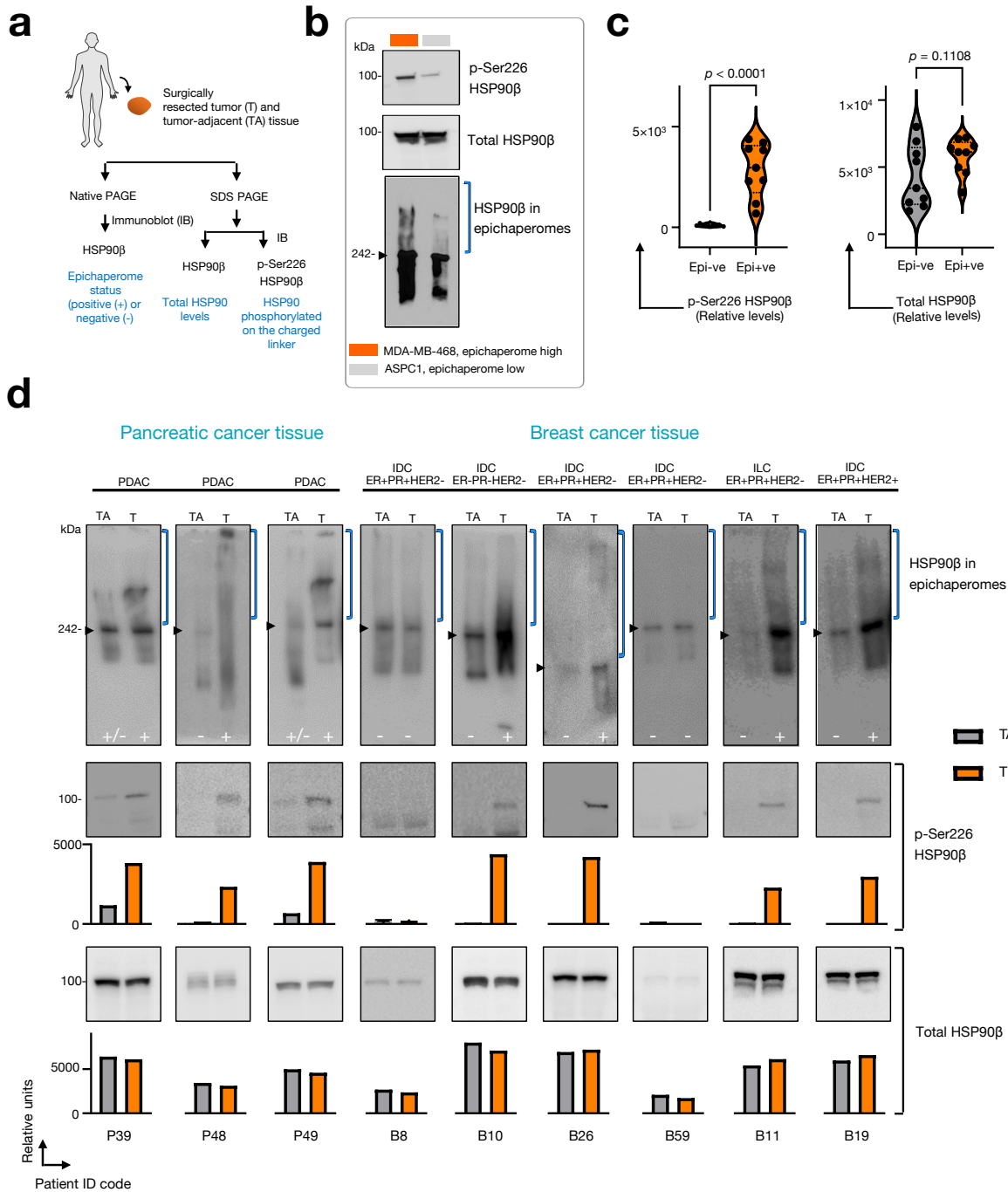


Figure 10. Human tissues positive for epichaperomes exhibit p-Ser226 HSP90 β positivity, and conversely, those negative for epichaperomes show no or negligible p-Ser226 signal within HSP90's charged linker. **a** Cartoon illustrating the processing of human tissue for biochemical analyses. Both tumor (T) and tumor adjacent (TA) tissues, determined by gross pathological evaluation to be potentially non-cancerous, were harvested and analyzed. **b** MDA-MB-468 breast cancer cells (epichaperome-high) and ASPC1 pancreatic cancer cells (epichaperome-low) served as controls for assessing p-Ser226 HSP90 levels. **c** The graph presents the relationship between epichaperome positivity and HSP90 Ser226 phosphorylation for tissues described in panel a. Data represent mean \pm s.e.m., with $n = 9$ tumor (T) and $n = 9$ paired tumor-adjacent (TA) tissues classified based on epichaperome positivity or negativity, as determined by Native PAGE (see panel d); unpaired two-tailed t-test. **d** Detection of epichaperomes through native-PAGE (top), and of p-Ser226 HSP90 (middle) and total HSP90 (bottom) by SDS-PAGE, followed by immunoblotting, in tissues from the indicated patient specimens, as in panel a. Blue brackets indicate the approximate position of epichaperome-incorporated HSP90. Note: Obtaining genuinely "normal" tissue adjacent to tumors presents challenges, especially in the case of pancreatic tissue. The relatively small size of the organ and the nature of surgical procedures for pancreatic cancer often lead to the collection of normal samples in close proximity to the tumor. It's crucial to acknowledge that, due to these challenges, we designate potentially normal tissue as tumor-adjacent tissue, recognizing that it may not entirely reflect a truly normal tissue state. PDAC, Pancreatic Ductal Adenocarcinoma; IDC, Invasive Ductal Carcinoma; ILC, Invasive Lobular Carcinoma; ER, Estrogen Receptor; PR, Progesterone Receptor. Source data are provided as Source data file.

Supplementary Files

This is a list of supplementary files associated with this preprint. Click to download.

- [SupplementaryData1.xlsx](#)
- [SupplementaryData2.xlsx](#)
- [SupplementaryData3.xlsx](#)
- [SupplementaryData4.xlsx](#)
- [SupplementaryData5.xlsx](#)
- [SupplementaryData6.xlsx](#)
- [SupplementaryInformation03.01.2024.pdf](#)
- [SourceData.xlsx](#)